Doctoral Dissertation

Theoretical Studies on Hydrazine-Metal Surface Reactions

— Adsorption States and Decomposition Reactions —

(金属表面におけるヒドラジン分子吸着及び分解反応に関する理論的研究)

Fadjar Fathurrahman

July 2015

Graduate School of Engineering,
Osaka University

Abstract

Hydrazine (N_2H_4) is an inorganic chemical, which is important in various applications. It is mainly used as fuel (monopropellant) for rocket engines and satellites. Recently, hydrazine has been investigated for hydrogen generation and precious-metal-free direct hydrazine fuel cell. Catalytic decomposition of hydrazine on solid surfaces, usually metal catalysts, is an important process in these applications. In practical applications, the decomposition reaction should be controlled. In order to control these reactions, atomistic level understanding of hydrazine-metal surface reactions is important. Significant to this is the information about the adsorption process and decomposition reaction pathways, which can be provided, at least partially, by theoretical studies based on computational methods.

In this dissertation, first-principles computational method based on density functional theory (DFT) is used to study several aspects of hydrazine-metal surface reactions. These aspects include hydrazine adsorption configurations on metal surfaces, N—N and N—H bond cleaving, and its dehydrogenation reaction pathways.

In the first chapter, background information about hydrazine applications and its decomposition reactions, along with the objectives and the scope of this work, are presented. In the second chapter, the basic theory and computational methods used in this work are described.

In the third chapter, the adsorption configurations of hydrazine on various close-packed metal surfaces of $3d$, $4d$, and $5d$ metals are discussed. Two kinds of adsorption configurations are considered: the top and bridging configurations. It is found that for most metal surfaces, the bridging configurations are preferred over the top configurations. Going from metals at the left to the right side of the periodic table, the preference for the bridging configurations over the top configurations becomes weaker. Electronic structure of the adsorbed hydrazine is also analyzed and it is found that the interaction with the surface is dominated by HOMO-derived and HOMO-1-derived orbitals of hydrazine. The results presented in this chapter provide comprehensive information about the relative stability of hydrazine adsorption conformations on close-packed metal surfaces, which are not yet available in the literature. These information are expected to be useful for future experimental works of hydrazine adsorption configurations on metal surfaces.

In the fourth chapter, the N—N bond cleaving of hydrazine is discussed, focusing on several $3d$ metal surfaces: Fe(110), Co(0001), Ni(111), Cu(111), and Zn(0001). It is found that the activation energy for N—N bond cleaving increases from Fe(110) to Zn(0001). By analyzing the electronic structure of the transition states, it is found that the increasing activation energy in N—N bond cleaving process is related to the occupation of LUMO-derived molecular orbitals of hydrazine at the transition state. We extend our study to other metal surfaces and establish a linear relation-

ship between activation energy and reaction energy (difference between energy of products with reactants), which is also known as the Brønsted-Evans-Polanyi (BEP) relationship. To the best of our knowledge, this relationship for the N—N bond cleaving of hydrazine has not been reported before. We show that this relationship can be extended to include other energetic parameters, such as adsorption energies, suggesting the applicability of the recently proposed *extended* BEP relationship. This BEP relationship is expected to be useful in estimating activation energy of N—N bond cleaving for other systems, such as alloy surfaces, utilizing only the adsorption energy as the input.

In the fifth chapter, the first N—H bond cleaving of hydrazine is discussed with the focus on late $3d$ metal surfaces and compared with the N—N bond cleaving. It is found that the activation energy for N—H bond cleaving increases from Fe(110) to Zn(0001). This trend is similar to the trend for N—N bond cleaving. For all surfaces, the N—H bond cleaving is found to have a higher activation energy as compared to that for the N—N bond cleaving. From electronic structure analysis, we also found that the occupation of LUMO-derived molecular orbitals of hydrazine at the transition state is responsible for the increasing trend in activation energy. The BEP relationship and the extended BEP relationship for the N—H bond cleaving of hydrazine are also investigated for several metal surfaces. Taking into account the results of the previous chapter, it is found that the N—N bond cleaving is more preferable than the N—H bond cleaving. This N—N bond cleaving is suggested to be responsible for the presence of adsorbed NH_2, which is reported in many experimental studies.

In the sixth chapter, the reaction pathways of hydrazine dehydrogenation on Ni(111) surface, which is of special interest, is presented. Two dehydrogenation pathways are considered: direct and NH_2-assisted dehydrogenation. In direct dehydrogenation, the N—H bonds of hydrazine are cleaved directly, which results in H atom adsorption on the surface. Meanwhile, in NH_2-assisted dehydrogenation, the N—H bonds of hydrazine are cleaved by H transfer from hydrazine to the adsorbed NH_2 fragments, which results in ammonia formation. NH_2-assisted dehydrogenation is found to have significantly lower activation energy as compared to the direct dehydrogenation. This result suggests that NH_3 formation is favorable on Ni(111). The results in this chapter are similar to the results of previous computational studies of hydrazine dehydrogenation on Ir(111) and Rh(111).

In conclusion, we have provided new information regarding hydrazine adsorption, a comparison between N—N and first N—H bond cleaving of hydrazine, and the dehydrogenation reaction pathways of hydrazine on Ni(111) surface. This information can be used as a guide to control the decomposition reaction of hydrazine and as a foundation for further studies of hydrazine-metal surface reactions in more complicated environments. As an example of the application of the results presented in this work, we consider the direct hydrazine fuel cell. In this type of fuel cell, the decomposition of hydrazine should be minimized because it does not produce electricity and will lead to lower utilization of hydrazine. Ammonia production is regarded as a sign of this inefficiency. We propose NiZn alloy as a catalyst which has low ammonia production and thus can be used for a more efficient direct hydrazine fuel cell.

Contents

List of Tables

List of Figures

CHAPTER 1

Introduction

1.1 Background of the problem

Adsorption and reactions of hydrazine (N_2H_4) on solid surfaces are important phenomena because of their relevance in several energy-related applications. As an example, hydrazine recently has been investigated as fuel in direct hydrazine fuel cell (DHFC) [1–5]. This type of fuel cell is interesting because it uses non-precious metal catalyst and has potential application in automotive industry. Hydrazine has been also investigated in carbon-free hydrogen storage and generations because of its high hydrogen content [6–8]. Moreover, hydrazine is also used widely as propellant for rocket engines [9] and as a reducing agent in chemical synthesis [10]. Most of those applications involve interaction between hydrazine and solid surface which usually act as a catalyst. Therefore, understanding the interaction between hydrazine and solid surfaces is required for better catalyst design.

On solid surfaces, hydrazine generally decomposes into ammonia (NH_3), nitrogen (N_2), and hydrogen (H_2). This decomposition reaction is a central aspect in the aforementioned applications. Depending on reaction conditions and nature of the catalyst surface, the stoichiometric amount of each decomposition product might vary. This decomposition reaction is usually described by two reactions, the complete decomposition

$$N_2H_4 \longrightarrow N_2 + 2\,H_2 \tag{1.1}$$

and incomplete decomposition

$$3\,N_2H_4 \longrightarrow N_2 + 4\,NH_3. \tag{1.2}$$

Sometimes, these two reactions are combined into one reaction [11]

$$3\,N_2H_4 \longrightarrow 4(1-x)NH_3 + (1+2x)N_2 + 6xH_2 \tag{1.3}$$

with $0 \leq x \leq 1$. The reaction pathways of the decomposition as described by 1.3 are possibly complex and involve a lot of possible elementary steps. Experimentally, there is no consensus yet regarding the reaction pathways of this decomposition reaction.

Due to its importance, hydrazine-solid surfaces reactions has been studied extensively. Most of these studies are of experimental nature, focusing on the hydrazine decomposition reactions on metals. Perhaps the earliest systematic study of hydrazine decomposition on metal was done by

Aika [12]. This study found that N_2 and NH_3 are the main products of hydrazine decomposition reactions metal surfaces. Another systematic study of hydrazine decomposition reaction was also done by Maurel [13]. This study found that N_2 is always formed from a single hydrazine molecule. This result may be attributed to the fact that none of the actual mechanism involve N—N bond breaking or it is simple associated with lack of mobility or diffusion of reaction intermediates. Other studies include the investigations of hydrazine decomposition on specific systems such as molybdenum films [14], tungsten films [15], supported iridium catalyst [16], aluminium [17], Ni(111) [18], Rh(100) [19], clean rhodium surface [20, 21], Pd(100) [22], Rh(111) [23], Pt(111) [24], Ni(100) [25], Ru(0001) [26], and alumina-supported iridium cluster [27, 28]. Other than on metals, studies of hydrazine decomposition on semiconductor were also done, for examples on GaAs(100) [29], Si(100) [30], molybdenum nitride [31], Si(111) [32], iron nitride [33], and tungsten carbide [34]. A common result of those studies is that N_2 and NH_3 are the main products of the decomposition reactions, i.e., the Reaction (1.2) is the dominant one. Those studies also confirmed the presence of NH_2 as one of the reaction intermediates.

Despite these numerous studies, several fundamental aspects of hydrazine-surface interaction are not yet established, especially regarding the adsorption structures or configurations and the decomposition reaction pathways. The adsorption of hydrazine is one aspect of the interaction between hydrazine and solid surfaces. Determining the adsorption sites, configurations, and energies are important tasks to characterize this phenomenon. Recently, several theoretical studies based on first-principles calculations have been done to address these problems. Most of these studies focus on adsorption process of hydrazine on clean transition metal surfaces such as Cu(111), Cu(100), Cu(110) [35], Ni(100) [36], Pt(111) [37], Ni(111) [38], Co(0001), and Pd(111) [39]. From these studies it was found that hydrazine may adsorb in the top configuration, where one N atom of hydrazine bonds to one surface atom, or the bridging configuration, where each N atom bonds to one surface atom. These studies concluded that hydrazine will prefer to adsorb in the top configuration than the bridging configuration. However, on other surfaces these information are not yet available and it is desirable to extend these studies to include other surfaces to provide more comprehensive view of hydrazine adsorption metal surfaces. Other theoretical studies [40–42] focus on the reaction path of hydrazine decomposition reactions.

Another important question regarding initial stages of hydrazine decomposition is which bonds will be cleaved first: the N—N or N—H bond of hydrazine. It has been previously reported that in the gas phase, the dissociation energy of N—N bond of hydrazine is about 2.96 eV, while that of N—H is 3.73 eV [9]. From these data it might be suggested that the N—N bond will be more easily cleaved than the N—H bond of hydrazine. Several computational studies have indeed shown that the N—N bond cleaving is more preferable than the first N—H bond of hydrazine on Ir(111) [41] and Rh(111) [42]. It is also desirable to compare the reactivity of N—N and N—H bond cleaving of hydrazine on other metal surfaces to provide a more extensive view of these processes.

In this dissertation, we will address some of the aforementioned problems. Specifically, we will study the adsorption and N—N and N—H bond cleaving of hydrazine using first-principles calculations. Further N–H bond cleaving of N_2H_x fragment ($x = 1, 2, 3$), will also be investigated. The results obtained in this work are expected to be useful in controlling the decomposition of

hydrazine on metal surfaces. Direct hydrazine fuel cell is one important application of hydrazine. In this type of fuel cell, the decomposition reactions of hydrazine should be minimized, because in these reactions hydrazine is consumed without producing any electricity. Ammonia production is regarded as a sign of inefficient utilization of hydrazine and thus should be minimized [3].

1.2 Objectives

The objectives of this dissertation is to find the answers of the following questions:

- What are the adsorption configurations of hydrazine on metal surfaces? How are they different from one surface to another?
- How is the reactivity of metal surfaces towards N—N and N—H bond cleaving of hydrazine?
- How does the dehydrogenation of hydrazine proceed? We will specifically consider two dehydrogenation pathways of hydrazine which are proposed in the previous studies [41, 42].

1.3 Scope

In this dissertation, we limit our study to close-packed surfaces of metals. We also used fixed coverage of hydrazine is used. We will used the activation energy (minimal energy required for a reaction to proceed) as a measure of the surface reactivity towards certain reaction steps of hydrazine decomposition. Dehydrogenation of hydrazine will be investigated on Ni(111) surface due to its importance as a non-precious-metal catalyst for hydrogen generation from hydrazine [6].

1.4 Outline

This dissertation consists of seven chapters. The first chapter gives basic information and background of the problem. In the second chapter we will discuss briefly the basic theory and computational methods used in this dissertation. In the third chapter we will discuss adsorption of hydrazine on metal surfaces. The fourth and fifth chapters are devoted to N—N and N—H bond cleaving of hydrazine, respectively. The dehydrogenation pathways of hydrazine will be discussed in the sixth chapter. Important concluding remarks and a way to minimize NH_3 production will be given in the seventh chapter.

CHAPTER 2

Theoretical methods

This chapter is intended as a brief review of theoretical methods used in this dissertation. We first give a review of density functional theory and its implementation in plane wave basis set. We also give a brief review of the method used to estimate activation energy of an elementary reaction step. The last section of this chapter, we give the computational details for the all calculations that are done in this work.

2.1 Density functional theory (DFT)

The total energy E of a system of N interacting electrons and can be found by solving the time-independent Schrödinger equation

$$\hat{H}\ \Psi\left(\mathbf{r}_1,\ldots,\mathbf{r}_N\right) = E\ \Psi\left(\mathbf{r}_1,\ldots,\mathbf{r}_N\right) \tag{2.1}$$

with the Hamiltonian (in atomic Hartree unit)

$$\hat{H} = \left(-\frac{1}{2}\sum_i \nabla_i^2 + \sum_i V\left(\mathbf{r}_i\right) + \sum_{i\neq j}\frac{1}{|\mathbf{r}_i-\mathbf{r}_j|}\right). \tag{2.2}$$

$V_{\text{ext}}\left(\mathbf{r}_i\right)$ is an external potential which may be due to the atomic nuclei, external electric and/or magnetic fields, etc.

Due to the complexity of the many body electron wave function $\Psi\left(\mathbf{r}_1,\ldots,\mathbf{r}_N\right)$, solving equation 2.1 is very difficult. In the Kohn-Sham density functional theory (KS-DFT) [43, 44], the role of $\Psi\left(\mathbf{r}_1,\ldots,\mathbf{r}_N\right)$ is replaced by much a simpler quantity, namely the density $\rho(\mathbf{r})$ of electrons

$$\rho(\mathbf{r}) = \sum_i^N f_i\left|\psi_i(\mathbf{r})\right|^2 \tag{2.3}$$

where $\psi_i(\mathbf{r})$ are one-electron wave functions or orbitals, f_i are the occupations of the orbitals, and i is a set of quantum numbers used to label the orbitals. These orbitals are also called the Kohn-Sham orbitals. In KS-DFT, the total energy of a system of interacting electrons is written as a functional

of the electron density $\rho(\mathbf{r})$

$$E[\rho] = T_s[\rho] + \int V_{\text{ext}}(\mathbf{r})\rho(\mathbf{r})\ \mathrm{d}\mathbf{r} + E_{\text{H}}[\rho] + E_{\text{xc}}[\rho]. \tag{2.4}$$

In Equation (2.4), T_s is the kinetic energy of non-interacting electrons

$$T_s = \sum_{i=1}^{N} \int \psi_i^*(\mathbf{r}) \left(-\frac{1}{2}\nabla^2\right) \psi_i(\mathbf{r}), \tag{2.5}$$

E_{H} is the Hartree energy

$$E_{\text{H}}[\rho] = \frac{1}{2} \int\int \frac{\rho(\mathbf{r})\rho(\mathbf{r}')}{|\mathbf{r}-\mathbf{r}'|}\ \mathrm{d}\mathbf{r}\ \mathrm{d}\mathbf{r}', \tag{2.6}$$

and E_{xc} is the exchange-correlation energy. The explicit for form of E_{xc} term is not known exactly. In practice, an approximation of E_{xc} must be used. The simplest approximation of E_{xc} is the local-density approximation (LDA), which takes the following form

$$E_{\text{xc}}^{\text{LDA}}[\rho] = \int \rho(\mathbf{r})\epsilon_{\text{xc}}^{\text{HEG}}.\ \mathrm{d}\mathbf{r} \tag{2.7}$$

$\epsilon_{\text{xc}}^{\text{HEG}}$ is the exchange-correlation energy per particle of a homogeneous electron gas (HEG) of charge density ρ. The ground state total energy E_0 can be found by minimizing the functional (2.4).

The one-electron wave functions $\psi_i(\mathbf{r})$ can be obtained by solving the so-called Kohn-Sham equations:

$$\left(-\frac{1}{2}\nabla^2 + V_{\text{KS}}(\mathbf{r})\right) \psi_i(\mathbf{r}) = \epsilon_i \psi_i(\mathbf{r}) \tag{2.8}$$

with ϵ_i are one-electron energies and $V_{\text{KS}}(\mathbf{r})$ is the Kohn-Sham (effective) potential

$$V_{\text{KS}}(\mathbf{r}) = V_{\text{ext}}(\mathbf{r}) + \int \frac{\rho(\mathbf{r}')}{|\mathbf{r}-\mathbf{r}'|} + \frac{\delta}{\delta\rho} E_{\text{xc}}[\rho]. \tag{2.9}$$

The Kohn-Sham equations must be solved self-consistently.

2.2 Implementation of DFT using plane wave basis set

In this dissertation we are mainly interested in systems that are periodic. A periodic system is composed of a periodically repeated unit cell which can be described by three unit lattice vectors: $\mathbf{a}_1$, $\mathbf{a}_2$ and $\mathbf{a}_3$. These vectors may be combined into a 3×3 matrix $\mathbf{h}$ defined by

$$\mathbf{h} = [\mathbf{a}_1, \mathbf{a}_2, \mathbf{a}_3] \tag{2.10}$$

The unit cell volume Ω may be calculated as determinant of this matrix

$$\Omega = \det \mathbf{h} \tag{2.11}$$

In addition to the real space unit cell, a reciprocal unit cell can also be defined by three reciprocal unit lattice vectors: $\mathbf{b}_1$, $\mathbf{b}_2$ and $\mathbf{b}_3$. These reciprocal lattice vectors are related to the real space

unit cell by the equation

$$\mathbf{b}_i \cdot \mathbf{a}_j = 2\pi\delta_{ij} \tag{2.12}$$

or by the matrix equation

$$[\mathbf{b}_1, \mathbf{b}_2, \mathbf{b}_3] = 2\pi \left(\mathbf{h}^T\right)^{-1}. \tag{2.13}$$

Solution of Schrodinger equation in periodic system can be written as

$$\psi_{i,\mathbf{k}}(\mathbf{r}) = e^{\imath\mathbf{k}\cdot r} u_{i,\mathbf{k}}(\mathbf{r}). \tag{2.14}$$

The function $u_{i\mathbf{k}}(\mathbf{r})$ has periodicity of the system

$$u_{i,\mathbf{k}}(\mathbf{r}+\mathbf{L}) = u_{i,\mathbf{k}}(\mathbf{r}) \tag{2.15}$$

where $\mathbf{L}$ denotes any lattice vector. The so-called crystal vector, $\mathbf{k}$, is a set of three real numbers.

In order to solve the Kohn-Sham equations using numerical methods, we need to discretize or represent the Kohn-Sham orbitals with a suitable basis set. For periodic systems, the most natural choice is the plane wave basis set. A plane wave $f_{\mathbf{G}}^{\mathrm{PW}}(\mathbf{r})$ is characterized by its reciprocal lattice vector $\mathbf{G}$ and defined by the equation

$$f_{\mathbf{G}}^{\mathrm{PW}}(\mathbf{r}) = \frac{1}{\sqrt{\Omega}} \exp\left[\imath\mathbf{G}\cdot\mathbf{r}\right] \tag{2.16}$$

where the reciprocal lattice vector $\mathbf{G}$ is

$$\mathbf{G} = 2\pi(\mathbf{h}^T)^{-1}\mathbf{g} = i\mathbf{b}_1 + j\mathbf{b}_2 + k\mathbf{b}_3 \tag{2.17}$$

and $\mathbf{g} = (i, j, k)$ is a triple of integer values.

Any periodic function, for example the function $u_{i,\mathbf{k}}(\mathbf{r})$ of Equation (2.14), can be expanded using a plane wave basis set

$$u_{i,\mathbf{k}}(\mathbf{r}) = \frac{1}{\sqrt{\Omega}} \sum_{\mathbf{G}} u_{i,\mathbf{k}}(\mathbf{G}) \exp\left[\imath\mathbf{G}\cdot\mathbf{r}\right] \tag{2.18}$$

where $u_{i,\mathbf{k}}(\mathbf{G})$ are the expansion coefficients. The Kohn-Sham orbitals for periodic system then can be written as

$$\begin{aligned} \psi_{i,\mathbf{k}}(\mathbf{r}) &= \exp\left[\imath\mathbf{k}\cdot\mathbf{r}\right] u_{i\mathbf{k}}(\mathbf{r}) & (2.19)\\ &= \frac{1}{\sqrt{\Omega}} \sum_{\mathbf{G}} c_{i,\mathbf{G}+\mathbf{k}} \exp\left[\imath(\mathbf{G}+\mathbf{k})\cdot\mathbf{r}\right] & (2.20) \end{aligned}$$

where $c_{i,\mathbf{G}+\mathbf{k}}$ are the expansion coefficients. The limits of the reciprocal vector $\mathbf{G}$ used for Kohn-Sham orbital expansion is determined by the following criterion

$$\frac{1}{2}\left|\mathbf{G}+\mathbf{k}\right|^2 \leq E_{\mathrm{cut}} \tag{2.21}$$

where E_{cut} is a given cutoff energy. In practical calculations, it usually ranges from 10 to 25 Ha or

larger. Using plane wave basis set, the electron density $\rho(\mathbf{r})$ that will be calculated from Kohn-Sham orbitals can be written as

$$\rho(\mathbf{r}) = \frac{1}{\Omega}\sum_i \int f_{i,\mathbf{k}} c^*_{i,\mathbf{G}'+\mathbf{k}} c_{i,\mathbf{G}+\mathbf{k}} \exp\left[\imath(\mathbf{G}+\mathbf{k})\cdot\mathbf{r}\right] \mathrm{d}\mathbf{k} \tag{2.22}$$

$$= \sum_{\mathbf{G}} \rho(\mathbf{G}) \exp\left[\imath\mathbf{G}\cdot\mathbf{r}\right] \tag{2.23}$$

where $\rho(\mathbf{G})$ are expansion coefficients for electron density. In the last summation, the range is twice as that of Equation (2.20).

In the most physical systems, the external potential is due to atomic nucleus. This potential can be written as

$$V_{\mathrm{ext}}(\mathbf{r}) = \sum_I \frac{Z_I}{\mathbf{r}-\mathbf{R}_I} \tag{2.24}$$

where $\mathbf{R}_I$ and Z_I denote the nucleus position and its atomic number, respectively. In this case, we will have a divergence at the nucleus. This divergence will give problems for numerical implementation. The wave function will also oscillate strongly near the nucleus. To describe this strong oscillation, we need a lot of plane waves. This in turn will make the use of plane wave basis set impractical. To solve this problem, the potential of nucleus is replaced by an effective potential, which is also known as pseudopotential. The pseudopotential does not have divergences at the nuclei and this will result in a smoother wave function near the nucleus.

2.3 Nudged elastic band method

Nudged elastic band (NEB) [45] method is a method to find minimum energy path between two states (or images). The path is discretized by dividing it into several images which are connected via imaginary springs. This discretized path is also called elastic band. The i-th image is described by atomic coordinates which will be denoted as $\mathbf{R}_i$. The elastic band with $N+1$ will be denoted by $[\mathbf{R}_0, \mathbf{R}_1, \mathbf{R}_2, \ldots, \mathbf{R}_N]$, where the endpoints $\mathbf{R}_0$ and $\mathbf{R}_N$ are fixed and given by the energy minima corresponding to initial and final states.

In the NEB method, the total force acting on the i-th image is the sum of the spring force along the local tangent and the true force perpendicular to the local tangent

$$\mathbf{F}_i = \mathbf{F}_i^s|_{\parallel} - \nabla E(\mathbf{R}_i)|_{\perp} \tag{2.25}$$

where the true force is given by

$$\nabla E(\mathbf{R}_i)|_{\perp} = \nabla E(\mathbf{R}_i) - \nabla E(\mathbf{R}_i)\cdot\hat{\boldsymbol{\tau}}_i \tag{2.26}$$

In these equations, E is the energy of the system as function of all the atomic coordinates $\mathbf{R}_i$, and $\hat{\boldsymbol{\tau}}_i$ is the normalized local tangent at image i. The simplest estimate to this local tangent is the

normalized line segment between two adjacent images, $\mathbf{R}_{i+1}$ and $\mathbf{R}_{i-1}$, along the elastic band

$$\hat{\boldsymbol{\tau}}_i = \frac{\mathbf{R}_{i+1} - \mathbf{R}_{i-1}}{|\mathbf{R}_{i+1} - \mathbf{R}_{i-1}|} \tag{2.27}$$

A better estimate of the tangent is to bisect between the two unit vectors [46]

$$\boldsymbol{\tau}_i = \frac{\mathbf{R}_i - \mathbf{R}_{i-1}}{|\mathbf{R}_i - \mathbf{R}_{i-1}|} + \frac{\mathbf{R}_{i+1} - \mathbf{R}_i}{|\mathbf{R}_{i+1} - \mathbf{R}_i|} \tag{2.28}$$

and then normalize $\hat{\boldsymbol{\tau}} = \boldsymbol{\tau}/|\boldsymbol{\tau}|$. The spring force is given by

$$\mathbf{F}_i^s|_{\parallel} = k\left(|\mathbf{R}_{i+1} - \mathbf{R}_i| - |\mathbf{R}_i - \mathbf{R}_{i-1}|\right)\hat{\boldsymbol{\tau}}_i \tag{2.29}$$

where k is the spring constant. Using an optimization algorithm is used to move the images according to the force in Equation (2.25).

In the climbing image NEB (CINEB) [47] method, the regular NEB method is slightly modified to ensure rigorous convergence to a saddle point. Typically, after a few iterations with the regular NEB, the image with the highest energy $i_{\max}$ is identified. The force on this image is not given by Equation (2.25) but rather by

$$F_{i_{\max}} = -\nabla E\left(\mathbf{R}_{i_{\max}}\right) + 2\,\nabla E\left(\mathbf{R}_{i_{\max}}\right)|_{\parallel} \tag{2.30}$$

The climbing image moves up the potential energy surface along the elastic band and down the potential surface perpendicular to the band. As long as the CINEB method converges, the climbing image will converge to the saddle point.

2.4 Computational details

In this dissertation, DFT-based electronic structure calculations were carried out by using the Quantum ESPRESSO package [48]. Ultrasoft pseudopotentials [49] were used to treat interaction between electron and ionic cores. A list of pseudopotentials used in this work is given in Appendix A. Plane wave basis set with cutoff 30 Ry (1 Ry = 0.5 Ha $\approx$ 13.6 eV) for wave function and 200 Ry for electronic density were used. Marzari-Vanderbilt cold smearing [50] with width of 0.01 Ry are used to treat the occupation number.

All metals that are considered in this thesis have relatively simple bulk crystal structures: face-centered cubic (fcc), body-centered cubic (bcc), and hexagonal close-packed (hcp). We used the most stable surface orientation for each crystal structures: fcc(111), bcc(110), and hcp(0001). All metal surfaces were modeled using 3-layer slabs and 3×3 supercell, constructed using their respective lattice bulk constants. Atomic Simulation Environment (ASE) [51] was used to construct slab models for metal surfaces. In Figure 2.1 we show a comparison of such slab models for bcc(110), hcp(0001), and fcc(111) surfaces. Comparison of adsorption energies obtained by using 4-layer shows that the trend of adsorption energy is similar to that obtained by using 3-layer slab model. During geometry optimization, atoms at the bottom layer were fixed while other atoms were allowed

to relax in any directions.

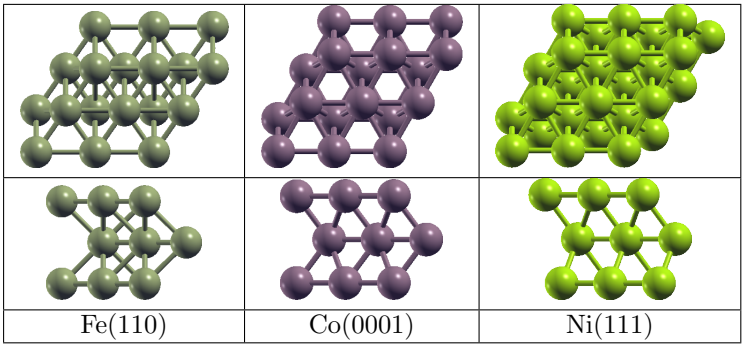

Figure 2.1: Top and side views of slab models used for Fe(110), Co(0001), and Ni(111).

A vacuum layer of about 20 Å and dipole correction was used to eliminate the interaction between periodic images of the slab. Brillouin zone sampling was done using $3 \times 3 \times 1$ Monkhorst-Pack grid. The PBE [52] exchange-correlation functional has been used for all calculations. Recent studies [53, 54] showed that PBE functional gives balanced description of the bulk structure of various transition metal elements. Spin polarization has been included in all calculations. DFT-D2 method [55–57] was used to account for dispersion force. The inclusion of DFT-D2 was found to be important for hydrazine adsorption on Cu surfaces [58] and is also expected to be important for other late *d*-block metals (located to the right of the periodic table) surfaces that are considered here.

Nudged elastic band (NEB) calculations were used to estimate activation energies. The reaction path was discretized using 8 images. Climbing image version of NEB (CINEB) was used to improve the transition state search. To verify that we have obtained the transition state, we did vibrational analyses and checked whether we have obtained one imaginary frequency for the corresponding structure.

Additional calculations of N—N bond stretching of hydrazine in the gas phase is done by Gaussian09 package [59] using basis set 6-31G(d,p) and B3LYP level theory. The resulting energy levels of hydrazine obtained using this setting is qualitatively similar to the ones obtained using plane wave calculation. Gaussian09 provides a *built-in* facility to extract the orbital coefficients and their real space 3D data. This enables the visualization of the orbitals and their nodal characteristics. However this facility is usually not provided in a plane wave DFT package. To obtain the visualization of Kohn-Sham orbitals in a plane wave DFT package we take the plane wave coefficients for a certain orbital (characterized by band index and $\mathbf{k}$-vector) and transform them from reciprocal space to real space using inverse FFT. The real or imaginary part of it can then be visualized to give us information about its nodal properties. In Chapter 5, we include calculation of MO-projected density of states. At the time of the writing of this dissertation, the tool to calculate this quantity is not available in Quantum Espresso distribution. This quantity can be calculated from the coefficients of atomic orbitals projection. A detail of our implementation is given in Appendix B. Xcrysden package [60] has been used in the visualization of molecular structures and 3D data. Numerous plots are done using `matplotlib` package [61].

CHAPTER 3

Hydrazine adsorption on metal surfaces

This chapter is devoted mainly to discuss hydrazine adsorption on close-packed metal surfaces of $3d$, $4d$, and $5d$ metals. This chapter begins with a brief discussion in first section about hydrazine conformations and their electronic structures in the gas phase. In the second section, we characterize the adsorption of hydrazine by calculating their adsorption energies and N—M bond length, where M is surface atom. We also discuss the observed trend for adsorption energies and N—M bond length. In the third section, we discuss the electronic structure of adsorbed hydrazine, taking two adsorption configurations of hydrazine on Fe(110) surface. At the end of the chapter we give a summary of important results.

3.1 Hydrazine in gas phase

In the gas phase hydrazine has three conformations: *anti* (or *trans*), *cis*, and *gauche*. These conformations are depicted in Figure 3.1. In gas the phase, the *gauche* conformation is the most energetically stable one, followed by *anti* and *cis*. From calculations, the *gauche* conformation has about 0.12 and 0.34 eV energy differences with *anti* and *cis* conformations, respectively.

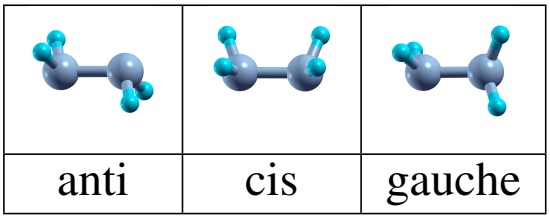

Figure 3.1: Conformations of hydrazine in gas phase

Hydrazine has 14 valence electrons which occupy 7 molecular orbitals (MOs). The energy levels of these MOs can be found in Figure 3.2. Note that we do not show the two lowest valence MOs in Figure 3.2 because they are too deep and not important in this discussion. Visualization and comparison of the five valence MOs of hydrazine in *anti*, *cis*, and *gauche* are given in Figure 3.3. For *anti* and *cis* we have used the molecular orbital notation for diatomic molecule, due to the similarity between them. For *gauche* conformation we have used the notation MOn, where n is index of valence MOs, to label the MOs.

From Figure 3.2, we can obtain a rough idea of the atomic orbital hybridization for each MO. We have placed the N—N bond of hydrazine along the x-axis so the 5σ MO of *anti* and *cis* and MO5

of *gauche* which have N—N bond character will be dominated by the contribution from nitrogen p_x. The 1π and $2\pi^*$ MOs of *anti* and *cis* which have N—H bonding character are composed almost exclusively by nitrogen p_y. The highest occupied MO (HOMO) and second highest occupied MO (HOMO-1) are composed mainly by nitrogen p_z. For *anti* and *cis*, HOMO is the $4\pi^*$ MO and HOMO-1 is the 3π MO. For *gauche* the HOMO and HOMO-1 are almost degenerate. The MO3 and MO4 of *gauche* are also almost degenerate. The HOMO of *anti* and *cis* have NH_2—NH_2 anti-bonding character while for *gauche* it is NH_2—NH_2 bonding character. This difference contribute to the stabilization of *gauche* conformation as compared to *anti* and *cis*.

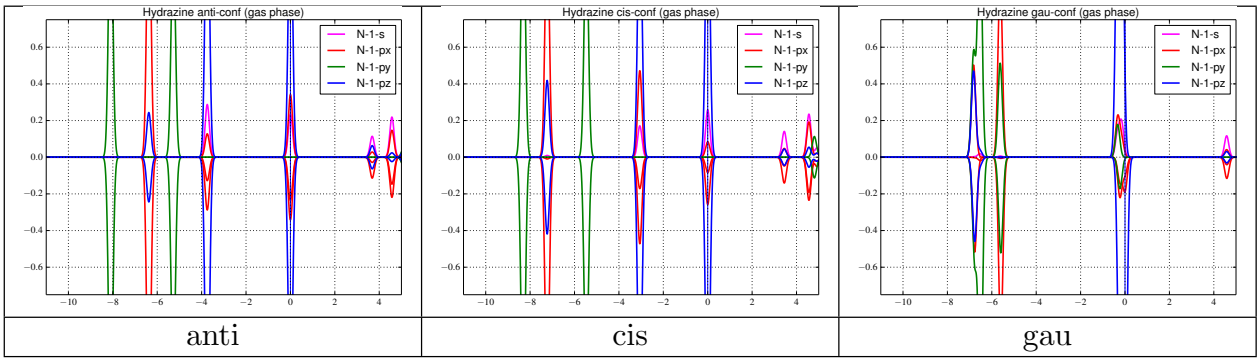

Figure 3.2: Density of states (DOS) of hydrazine in gas phase projected onto one N atom of hydrazine in *anti* and *cis* conformations. Unit of energy is eV. The levels have been broadened with smearing of 0.01 eV and shifted so that HOMO is located at 0 eV.

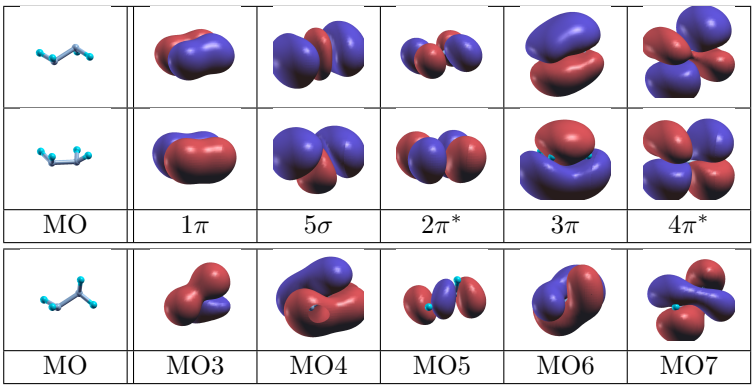

Figure 3.3: Visualization of occupied molecular orbitals of hydrazine. Colors red and blue are used to differentiate the signs (+/-) of the orbital.

3.2 Energetics and structure

The choice of initial guess for geometry optimization might affect the obtained adsorption configurations. In this work, several adsorption configurations of hydrazine were used as starting geometries. Such geometries can be found in Figure 3.4. The hydrazine molecule is positioned initially with an N—M (M is surface atom) distance of about 2.0 angstrom. Generally, these adsorption configurations are classified into the *top* configurations, where only one nitrogen atom of hydrazine is bonded

to surface atom, and the *bridging* configurations where both N atoms of hydrazine are bonded to two surface atoms. Letters A and B have been used to further differentiate slight variations in the adsorption configurations based on their relative hydrogen atoms arrangement. Some of them closely resemble the conformations of hydrazine in the gas phase: *top-A*, *top-B*, and *bri-A* are analogous to *anti*, *gauche*, and *cis* conformations in gas phase, respectively. Adsorption configuration *bri-B*, which does not have direct analog to the conformations in gas phase, is a slight distortion from *bri-A* configuration where NH_2 groups are rotated in opposite direction about N—N axis. For bcc(110) surface, there are two different bridge sites: the long and short bridge sites. In this case, long bridge site is chosen for simplicity. Some comments regarding the difference between long and short bridge sites of bcc(110) surfaces are given in Appendix C.

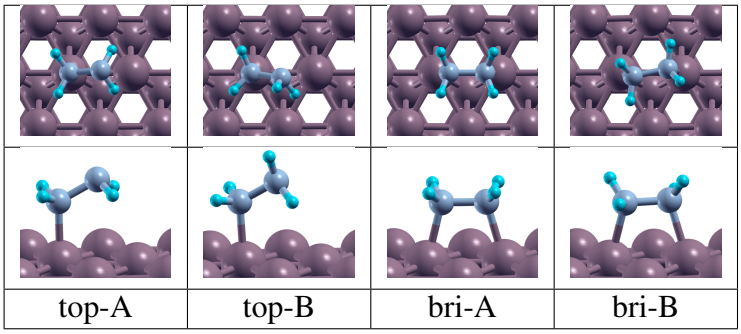

Figure 3.4: Adsorption configurations of hydrazine on metal surfaces. This figure shows hydrazine adsorption on Co(0001) surface. For other surfaces, the geometries are roughly similar.

Some notes regarding *top-B* configuration need to be mentioned here. With the choice of starting geometries described above, the optimized geometries can be obtained with relatively small number of relaxations steps. In other words, for most surfaces the results of geometry optimization were found to closely resemble the starting configurations. However, for Sc(0001), Y(0001), and La(0001), the *top-B* adsorption configuration was not found. On those surfaces, the *top-B* configuration relaxed to *bri-B*. This result might reflect the fact that the bridging configurations are strongly preferred on those particular surfaces as opposed to the top configurations.

Two quantities, the adsorption energy E_{ads} and the bond length $d_{\text{N}-\text{M}}$ between nitrogen atom of hydrazine and surface atom are used to characterize the adsorption. The adsorption energy is calculated using the following formula:

$$E_{\text{ads}} = E_{\text{mol/surf}} - E_{\text{surf}} - E_{\text{mol}} \tag{3.1}$$

where $E_{\text{mol/surf}}$ is the total energy of hydrazine adsorbed on surface, E_{surf} is the total energy of clean surface, and E_{mol} is the total energy of gas phase hydrazine molecule in *gauche* conformation. The adsorption energies of hydrazine and the N—M bond lengths on various metal surfaces are given in Table 3.1 and Table 3.2, respectively. In Figure 3.5 these quantities are plotted.

Several remarks about adsorption energies of hydrazine can be obtained. It is observed that for most surfaces, the bridging configurations have larger adsorption energies as compared to the top configurations. This is especially true for surfaces of early *d*-block metals (located to the left of the periodic table). This preference of bridging configurations becomes weaker as we go to the right of

Table 3.1: Adsorption energy of hydrazine in several configurations. Energies are given in eV.

Surface	top-A	top-B	bri-A	bri-B
Sc(0001)	-1.14	-	-1.46	-1.57
Ti(0001)	-1.39	-1.35	-1.71	-1.79
V(110)	-1.40	-1.34	-1.80	-1.90
Cr(110)	-1.50	-1.47	-1.73	-1.75
Fe(110)	-1.24	-1.20	-1.28	-1.34
Co(0001)	-1.44	-1.36	-1.47	-1.50
Ni(111)	-1.36	-1.27	-1.32	-1.35
Cu(111)	-1.13	-1.08	-0.94	-1.03
Zn(0001)	-0.65	-0.67	-0.29	-0.54
Y(0001)	-1.13	-	-1.36	-1.52
Zr(0001)	-1.37	-1.36	-1.66	-1.75
Nb(110)	-1.41	-1.40	-1.73	-1.83
Mo(110)	-1.57	-1.54	-1.72	-1.77
Ru(0001)	-1.84	-1.70	-2.01	-2.02
Rh(111)	-1.75	-1.73	-1.75	-1.77
Pd(111)	-1.54	-1.52	-1.34	-1.38
Ag(111)	-0.82	-0.81	-0.55	-0.80
Cd(0001)	-0.53	-0.58	-0.25	-0.54
La(0001)	-1.22	-	-1.33	-1.54
Hf(0001)	-2.13	-2.02	-2.40	-2.58
Ta(110)	-1.80	-1.74	-2.18	-2.26
W(110)	-2.00	-1.94	-2.05	-2.08
Re(0001)	-2.06	-1.94	-2.24	-2.25
Os(0001)	-2.33	-2.17	-2.50	-2.51
Ir(111)	-2.27	-2.06	-2.20	-2.20
Pt(111)	-2.44	-2.13	-2.13	-2.15
Au(111)	-1.42	-1.31	-1.06	-1.18

the periodic table. On the surfaces of late d-block metals (located to the right of the periodic table), top configurations have the larger adsorption energies instead. On the same surface, it is found that the configuration *bri-B* generally has larger adsorption energy than *bri-A*. It is also found that the configuration *top-A* generally has larger adsorption energy than *top-B*.

Several remarks about $d_{\mathrm{N-M}}$ also can be obtained. On the same surface, the bond length $d_{\mathrm{N-M}}$ is generally found to have the following order *top-A* < *top-B* < *bri-A* < *bri-B*. Within the same row (block) in the periodic table, going from the left to the right $d_{\mathrm{N-M}}$ becomes lower until it reaches a minimum and then rises again until the last element of the row. Within the same row in the periodic table, largest values of $d_{\mathrm{N-M}}$ are found on the surfaces of the last element on the row, i.e. on Zn(0001) of the 3d-block, Cd(0001) of the 4d-block and Au(111) of the 5d-block. The minima of $d_{\mathrm{N-M}}$ are found on Ni(111) of 3d-block, Pd(111) of the 4d-block and Pt(111) of the 5d-block.

A simple qualitative model [39] for hydrazine adsorption energy can used to explain the obtained trend. According to this model, contribution to adsorption energy can be divided into two contributions: the attractive and repulsive contributions. Qualitative explanation for the observed trend of adsorption energies of hydrazine across different surfaces can be obtained by noting that

Table 3.2: Distance between N atom of hydrazine and bonded surface atom. All values are given in angstrom.

Surface	top-A	top-B	bri-A	bri-B
Sc(0001)	2.299	-	2.340	2.363
Ti(0001)	2.184	2.210	2.220	2.251
V(110)	2.147	2.165	2.169	2.204
Cr(110)	2.108	2.123	2.131	2.146
Fe(110)	2.076	2.111	2.137	2.165
Co(0001)	2.050	2.091	2.081	2.108
Ni(111)	2.005	2.035	2.026	2.062
Cu(111)	2.064	2.089	2.108	2.163
Zn(0001)	2.197	2.260	2.377	2.503
Y(0001)	2.453	-	2.520	2.552
Zr(0001)	2.342	2.366	2.394	2.425
Nb(110)	2.281	2.305	2.332	2.362
Mo(110)	2.235	2.252	2.277	2.302
Ru(0001)	2.177	2.196	2.203	2.213
Rh(111)	2.122	2.122	2.153	2.168
Pd(111)	2.116	2.120	2.187	2.232
Ag(111)	2.333	2.381	2.431	2.528
Cd(0001)	2.472	2.520	2.663	2.824
La(0001)	2.578	-	2.662	2.714
Hf(0001)	2.287	2.315	2.367	2.394
Ta(110)	2.255	2.274	2.313	2.337
W(110)	2.231	2.252	2.302	2.318
Re(0001)	2.220	2.236	2.243	2.253
Os(0001)	2.172	2.187	2.202	2.207
Ir(111)	2.149	2.156	2.171	2.178
Pt(111)	2.110	2.126	2.158	2.153
Au(111)	2.284	2.333	2.422	2.512

there is competition between these attractive and repulsive contributions. The attractive E_{att} and repulsive E_{rep} contributions can be written as [62, 63]

$$E_{\text{att}} \propto -(1-f)\frac{V^2}{\epsilon_d - \epsilon} \tag{3.2}$$

$$E_{\text{rep}} \propto -(1+f)SV \tag{3.3}$$

where f and ϵ_d stand for d-band filling and center, respectively. V and S denote the coupling and overlap matrix element between adsorbate orbital and d-band of surface, respectively. The magnitude of overlap matrix can be taken to be proportional to the coupling matrix, $S \approx -\alpha V$, where α is a constant. The adsorption energy can then be written as $E_{\text{ads}} = E_{\text{att}} - E_{\text{rep}}$. The attractive interactions E_{att} will be larger for surfaces with low filling of d-band or lower ϵ_d. Meanwhile, the repulsive interaction E_{rep} will be larger for surfaces with high filling of d-band and higher ϵ_d. Surfaces of elements that are located to the left of periodic table will generally have larger E_{att} due to smaller d-band filling f. However, we can not expect that the trend will be monotonous (adsorption

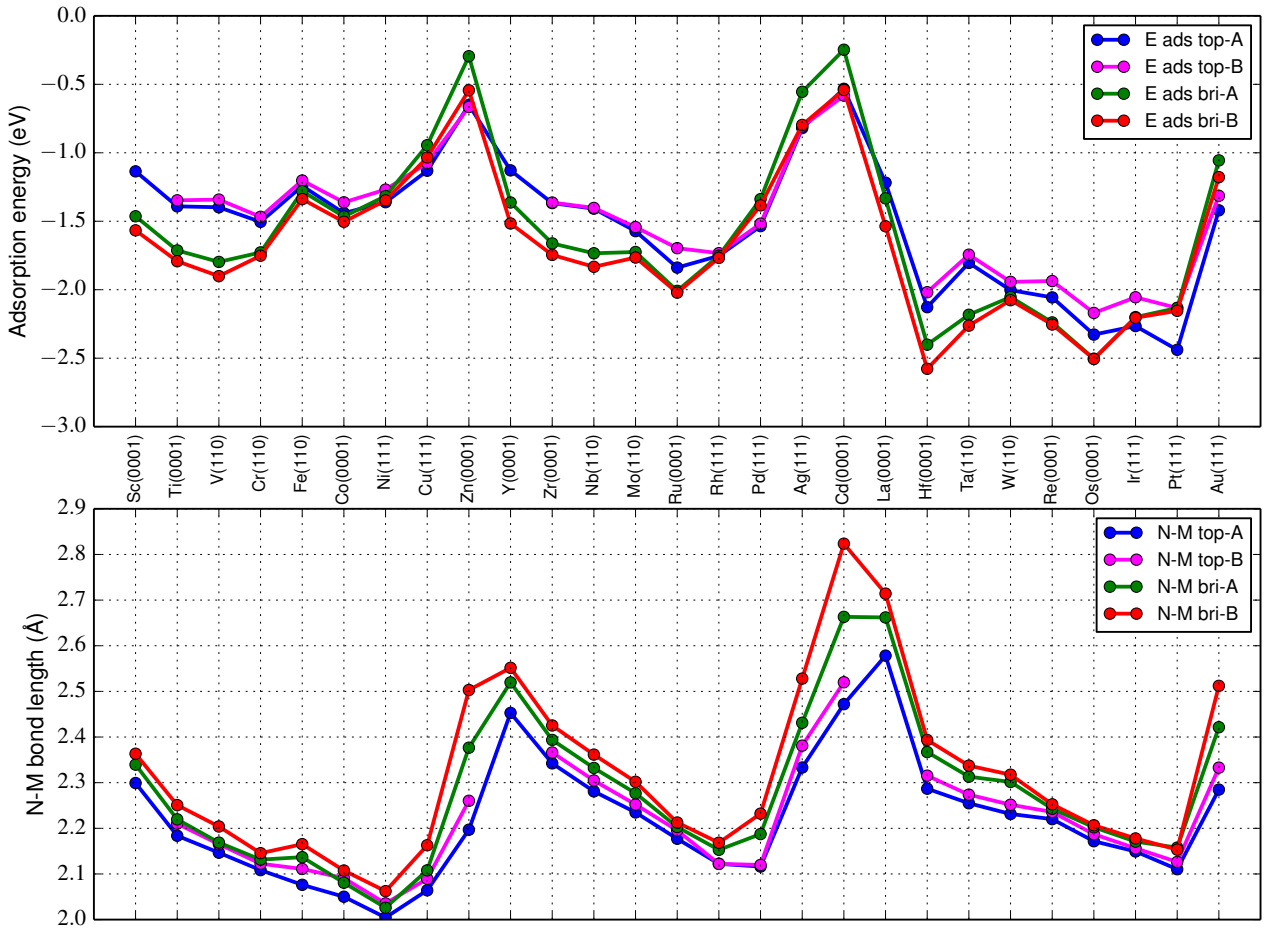

Figure 3.5: Adsorption energies (upper) and distance of bonded N atom of hydrazine with surface atom (lower). Note that data for *top-B* configuration on Sc(0001), Y(0001), and La(0001) have been skipped.

energy always more negative as we go to the left of periodic table) due to other factors such as the coupling matrix elements V, which in general do not possess certain trends across different elements in periodic table.

Besides the ϵ_d and coupling V, the overlap S between orbitals of adsorbate and surface atom will also affect E_{rep}. From geometrical considerations we can deduce the following trend of overlap among various adsorption configurations: *top-A* < *top-B* < *bri-A* < *bri-B*. Larger overlap will result in larger E_{rep} between electronic states of adsorbate with surface. To minimize this repulsion, adsorbate usually will move outward from the surface and this is reflected by the longer bond length. This is observed in the case of hydrazine adsorption where the larger the overlap the longer N—M distance (i.e., the *bri-B* configuration has the longest and *top-A* configuration has the shortest N—M bond). However, a larger overlap will also allow more interactions between adsorbate and surface. For example, in the case of hydrazine adsorption, bridging configurations have larger overlap, which also enables hydrazine to make bonds with two surface atoms as compared to top configurations, where only it only makes one bond with surface atom. So, the magnitude of E_{att} of bridging configurations (larger overlap) generally will also be larger than top configurations. However, if the energy gain obtained by this attractive attraction is less than the repulsive one

then adsorption energies of bridging configurations will be smaller than that of top configurations. This is found to be the case for surfaces of elements that are located to the right of periodic table. For surfaces of elements that are located to the left of periodic table, the energy gain by attractive interactions can overcome the repulsive one and the bridging configurations are found to have larger adsorption energies as compared to top configurations.

In the following, comparison with several previous theoretical results are given. The comparison is made mainly by comparing the trend of adsorption energies among different adsorption configurations.

The trend of adsorption energies magnitude among surfaces in one row: Co(0001) > Ni(111) > Cu(111) and in one column: Ni(111) < Pd(111) < Pt(111) that was reported earlier [39] is reproduced here. The adsorption configuration *top-A* (which is called *ads-anti* in that publication) was also found to have the largest adsorption energy on those surfaces. An exception is found for Co(0001) where the *bri-B* has slightly more negative adsorption energy than *top-A*. This difference might be attributed to the inclusion of dispersion force in the present study.

On Ir(111) [41], it was found that hydrazine has two adsorption configurations which resemble the *top-B* and *bri-B* with adsorption energies of 1.66 and 1.91 eV, respectively. The trend of relative stability between the adsorption configurations, i.e. bridge configurations is energetically more stable than top configurations, is different from the one obtained here.

On Rh(111) [42], it was found that hydrazine has two adsorption conformations which resemble *top-B* and *bri-B* with close adsorption energies of 1.14 eV and 1.11 eV, respectively. In that study, the trend of stability is also different from the one obtained here. However, the result that the two adsorption configurations have small adsorption energy difference is also obtained in the present work (0.04 eV energy difference between *top-B* and *bri-B*).

In the previous study of hydrazine adsorption on various low index copper surfaces [35], it was found that the top configurations have the largest adsorption energies on Cu(111). Recent study [58] included dispersion force and reconfirmed that the top configuration has the largest adsorption energy on Cu(111), although the bridging configuration might be preferred on other facets such as Cu(110). Their results are similar to the results obtained in the present study for Cu(111).

Note that in the present study, the coverage of hydrazine is not varied; we only consider the case of one molecule of hydrazine put on 3×3 supercell. It should be remembered that the adsorption configuration of hydrazine might also be dependent on the surface coverage. Particularly in high coverage systems, hydrazine-hydrazine interactions, especially the hydrogen bonds between hydrogen and nitrogen of neighboring hydrazine molecules can play important role in determining the adsorption configurations. While such possibility is out of the scope of the present study, it is very interesting and will be a subject of future studies.

3.3 Electronic structure of adsorbed hydrazine

In this section, we will consider an example electronic structure of adsorbed hydrazine. We will specifically consider the *top-A* and *bri-B* adsorption configurations of hydrazine on Fe(110) surface.

Fe(110) is chosen because it is located near the middle of *d*-block metals. For other surfaces we can do a similar kind of analysis. We will focus on the general features of the electronic structure of hydrazine adsorbed on metal surfaces.

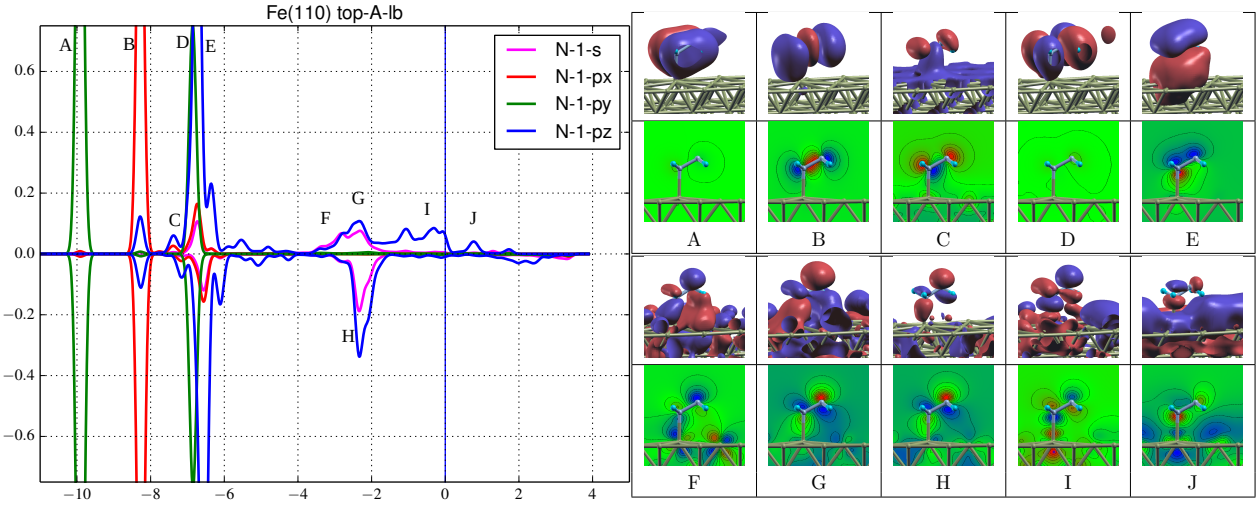

Figure 3.6: DOS projected onto N atom for adsorption configuration *top-A* and visualization of several adsorbed hydrazine molecular orbitals at several energy levels. Fermi level is at 0 eV.

In Figure 3.6 density of states (DOS) projected on adsorbed nitrogen atom of hydrazine in *top-A* configuration is shown. Several peaks or states have been labeled by letters A–J. Figure 3.6 also gives the visualization of the molecular orbitals corresponding to those peaks. The contour plots of these molecular orbitals are also given to show the interaction between Fe and nitrogen atoms. We can see that the state A is essentially the same as the 1π MO of gas phase hydrazine. No contribution from surface atoms is observed for this state. State B is the same as the 5σ MO of gas phase hydrazine. For state B, no contribution from surface atoms is observed. Thus for state A and B, no mixing or hybridization of hydrazine molecular orbitals with surface orbitals. State C, however, has contribution from surface atoms, presumably from the delocalized *sp*-orbitals of Fe. Thus, state C can be regarded as result of the interaction between 5σ MO of gas phase hydrazine and *sp*-orbitals of Fe surface. State D is the same as the $2\pi^*$ MO of gas phase hydrazine. Just like the states A and B, this state also does not mix with the orbitals from surface atoms. State E is analogous to LP orbital of gas phase. However, polarization of this molecular orbitals toward surface atoms can be observed. Thus, this state can be identified as dative-like bond between hydrazine and surface atom. Recall that the dative bond is a bond type where the bonding electron pair come from the same atom. Meanwhile, states F–J are mainly dominated by interaction between HOMO of hydrazine with surface orbitals, mainly the *d* states, resulting in bonding and anti-bonding orbitals. Some of them clearly show the symmetry of surface orbitals. For instance, state F shows bonding orbital due to d_{xy} and state I and J show anti-bonding orbital due to d_{z^2}. The mixing between atomic orbitals are very strong as evidenced by more balanced contribution between hydrazine and surface atoms.

In Figure 3.7 the projected DOS for *bri-B* configuration is given and several peaks or states have been labeled by letters A–J. States A and B of this configuration have same features as states A

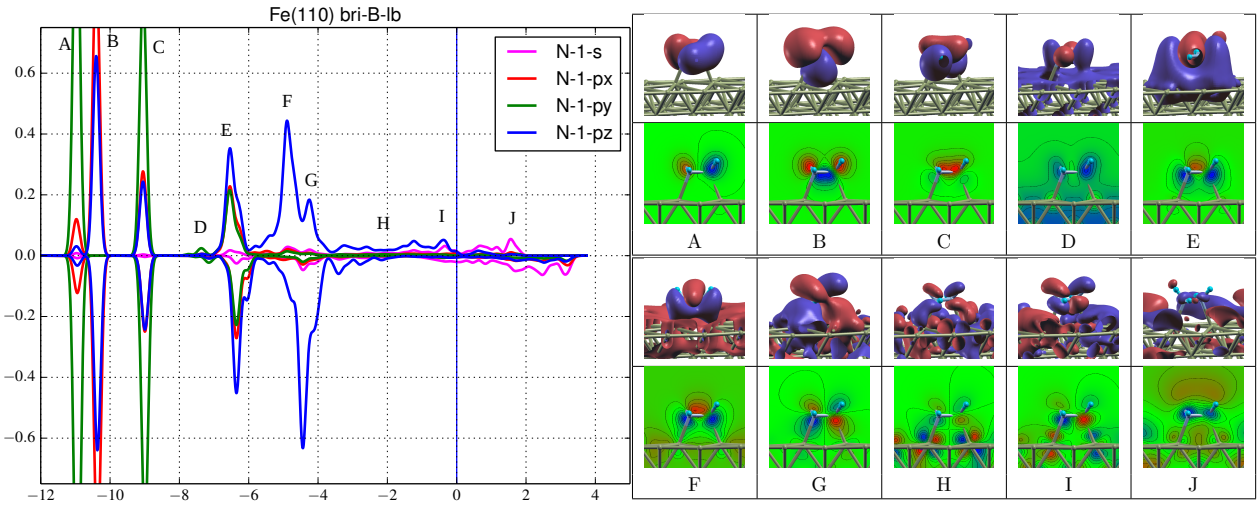

Figure 3.7: DOS projected onto N atom for adsorption configuration *bri-B* and visualization of several adsorbed hydrazine molecular orbitals at several energy levels. Fermi level is at 0 eV.

and B of *top-A* configuration because they represent a π and σ bonding, respectively. They also do not hybridize with surface atomic orbitals. State C is not a π anti-bonding orbital because it has bonding characteristic between two NH_2 fragments of hydrazine. State D has bonding characteristic with surface. It has similar feature as state C of *top-A* configuration that they both interact with *sp*-orbitals of surface. State E is the state derived from HOMO-1 of hydrazine which has dative bonding characteristic with surface. This state is analogous to the state E of *top-A* configuration. State F has the same characteristic as state E, however with the contribution of delocalized *sp*-orbitals of surface. States G, H, and I interact strongly with the surface orbitals. They are the result of the interaction between HOMO of hydrazine and the *d*-orbitals of surface atoms. Just like in the case of *top-A* configuration, the symmetry of surface orbitals which contributes in the interaction can be clearly seen from the contour plot: state G has bonding contribution from d_{z^2} of Fe, state H has bonding contribution from d_{xz}, and state I has anti-bonding contribution from d_{z^2}. State J does not have any recognizable character with the occupied hydrazine molecular orbitals in gas phase. It is probably the result of the interaction between unoccupied molecular orbital of hydrazine and surface orbitals. It does not have significant bonding characteristic with surface.

From the preceding discussion, several points regarding the orbital interactions between hydrazine and Fe(110) can be made. First, besides interaction with the delocalized *sp*-orbitals of the surface, HOMO of hydrazine interacts strongly with surface *d*-orbitals and forms derived bonding and anti-bonding orbitals with respect to surface atoms. Second, HOMO-1 mainly interacts with surface atom via a dative-like bond. Third, lower molecular orbitals, such as 5σ, only interact with the delocalized *sp*-orbitals of the surface. For other surfaces we can find similar features as the ones already shown for Fe(110). The NH_2—NH_2 anti-bonding character of HOMO of hydrazine and its strong interaction with surface might be an indication that N—N bond cleaving is preferred when hydrazine adsorb in a bridging configuration.

3.4 Chapter summary

Here, we give a list of important findings in this chapter.

- On metal surfaces, the adsorption configurations of hydrazine can be classified into the *top* and *bridging* configurations.
- For most surfaces, the *bridging* configurations are found to be the most stable adsorption configurations. For close-packed surfaces of early *d*-metals (metals that are located at left sides of periodic table), the bridging configuration may be $\sim$0.5 eV more stable than the top configurations.
- Going from metals at left to right of periodic table, the preference for *bridging* configuration is generally decreasing. The *top* configurations are favored instead on the close-packed surfaces of late *d*-metal (metals that are located at the right sides of periodic table).
- Simple model proposed in the previous study to describe adsorption energy of hydrazine is used to find explanation for the trend of hydrazine adsorption configuration. Within this model, adsorption energy is divided into attractive and repulsive contributions. On early *d*-metals, attractive contribution can overcome the repulsive contribution such that the configuration with large overlap, i.e. the bridging configuration, has larger adsorption energy as compared to top configuration. Meanwhile, for late *d*-metals, the attractive contribution is not effective and the repulsive contribution dominate the interaction with surface. In such case, the configuration with small overlap (minimal repulsion) is favored instead.
- The interaction of hydrazine with surfaces is dominated by the HOMO and HOMO-1 derived orbitals.

The results in this chapter provide comprehensive information about relative stability of hydrazine adsorption conformations on close-packed metal surfaces which are not yet available in the literature. These information are expected to be useful for future experimental works of hydrazine adsorption configurations on metal surfaces.

CHAPTER 4

N—N bond cleaving of hydrazine

In this chapter, we consider the N—N bond cleaving of hydrazine. This reaction step is responsible for the NH_2 species that is detected in several experiments [64]. It is also regarded as one possible initial step of hydrazine decomposition. We start by discussing the energetics of the initial, transition, and final states of N—N bond cleaving on $3d$ metals. We also discuss several electronic structure characteristics of N—N bond cleaving on these surfaces. After discussing of the energetics and electronic structure aspects of N—N bond cleaving on $3d$ metal surfaces, we give extended results of N—N bond cleaving energetics on other surfaces. We discuss a useful linear relationship which can be used to estimate activation energies of N—N bond cleaving.

4.1 Energetics of the N—N bond cleaving

Hydrazine adsorbed molecularly in *bri-A* configuration has been used as initial geometry for CINEB calculation for all surfaces. For final structure, adsorption structure with two NH_2 fragments adsorbed on two bridge sites is used for Fe(110), Co(0001), Ni(111), and Cu(111). For Zn(0001), adsorption structure with two NH_2 fragments adsorbed on two top sites is used as the final structure. Except for Zn(0001), such ontop structure is not found by geometry optimization on other surfaces. Figure 4.1 shows the initial, final, and transition state structures found from CINEB calculations for Fe(110), Co(0001), Ni(111), Cu(111), and Zn(00001). It can be observed that the transition states for N—N bond cleaving closely resemble the initial structures, so they may be classified as early transition states.

The adsorption energies of these structures along with the activation and reaction energies for each surface are given in Table 4.1. The imaginary frequencies associated with N—N bond stretch at the transition state are also provided in Table 4.1. In Figure 4.2, adsorption energies of initial, transition, and final states are visualized. Except for Zn(0001), N—N bond cleaving is found to be exothermic process (has negative ΔE) for all surfaces. The activation energy for this process has the lowest value for Fe(110) and highest for Zn(0001).

Two geometry quantities, i.e. the distance between N—N atoms of hydrazine $d_{\mathrm{N-N}}$ and the distance between N atom of hydrazine and bonded surface atom $d_{\mathrm{N-M}}$ (M = Fe, Co, Ni, Cu,or Zn), are given in Table 4.2 and 4.3, respectively for initial and transition state. It is found that the distance $d^{\mathrm{IS}}_{\mathrm{N-N}}$ has increasing trend from Fe(110) to Zn(0001), with very close values obtained for Co(0001), Ni(111), and Cu(111). The distance $d^{\mathrm{TS}}_{\mathrm{N-N}}$ does not have similar trend as the distance

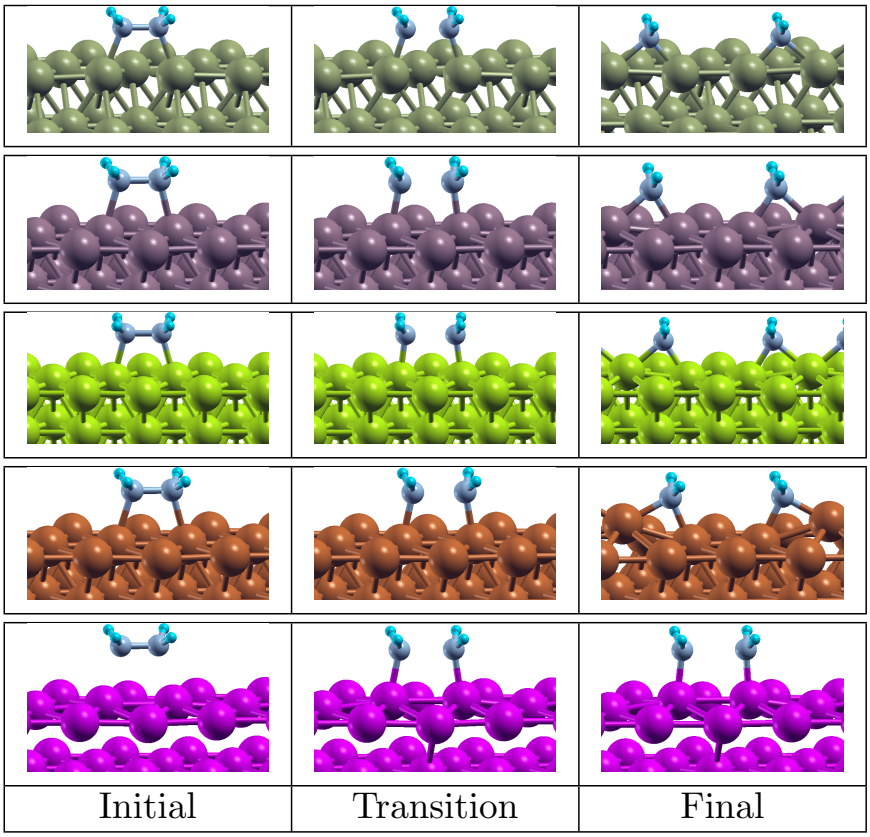

Figure 4.1: Initial, transition, and final states of N—N bond cleaving. From top to down: Fe(110), Co(0001), Ni(111), Cu(111), and Zn(0001).

Table 4.1: Calculated adsorption energies of initial E_{ini}, transition E_{TS}, and final structures E_{fin} of N—N bond cleaving of hydrazine. The reaction energy ΔE is calculated as $E_{\mathrm{fin}} - E_{\mathrm{ini}}$. All energies are given in eV and calculated relative to gas phase hydrazine in gauche conformation. The imaginary frequecies are given in cm^{-1}.

Surface	E_{ini}	E_{TS}	E_{fin}	ΔE	E_{act}	ν^{TS}
Fe(110)	-1.28	-1.05	-3.26	-1.96	0.23	504.4i
Co(0001)	-1.47	-1.08	-2.83	-1.36	0.39	337.0i
Ni(111)	-1.32	-0.83	-2.35	-1.03	0.49	334.6i
Cu(111)	-0.94	-0.35	-2.03	-1.09	0.59	516.8i
Zn(0001)	-0.29	0.62	0.42	0.71	0.91	168.1i

$d^{\mathrm{IS}}_{\mathrm{N-N}}$, however the lowest value is also obtained for Fe(110) and highest value for Zn(0001). Meanwhile, $d^{\mathrm{IS}}_{\mathrm{N-M}}$ has almost the same trend as adsorption energy E_{ini}. For all surfaces, $d^{\mathrm{TS}}_{\mathrm{N-M}}$ is found to be shorter than $d^{\mathrm{IS}}_{\mathrm{N-M}}$.

In order to find more insights into the N—N bond cleaving process, the activation energy is analyzed by E_{act} decomposing it into several parts according to the following equation [42, 65, 66]:

$$E_{\mathrm{act}} = E_{\mathrm{subs}} + E_{\mathrm{deform}} + \left(E^{\mathrm{TS}}_{\mathrm{A}} + E^{\mathrm{TS}}_{\mathrm{B}} - E^{\mathrm{TS}}_{\mathrm{int}}\right) - E^{\mathrm{IS}}_{\mathrm{AB}} \tag{4.1}$$

This decomposition scheme allows us to interpret the activation energy as various contributions

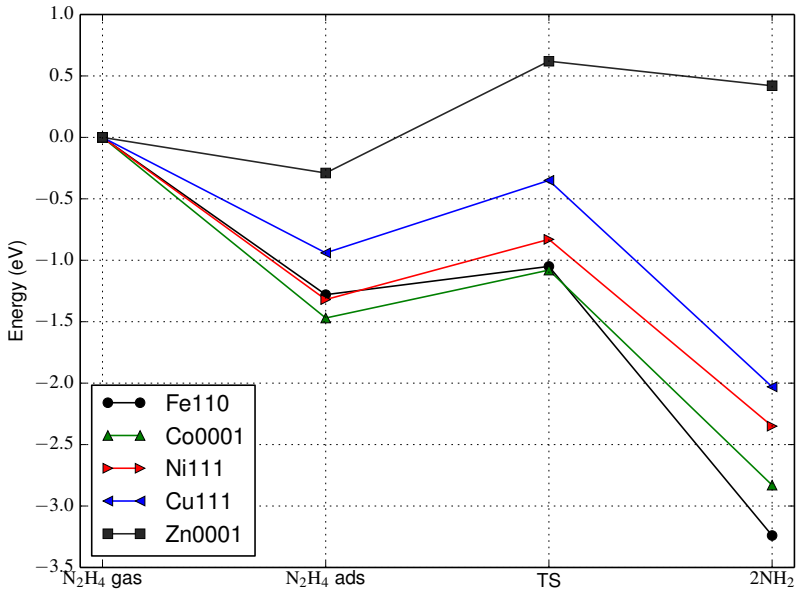

Figure 4.2: Energy diagram for N—N bond cleaving of hydrazine. The energies are calculated relative to sum of energies of isolated slab and gas phase hydrazine in *gauche* conformation.

Table 4.2: N—N bond distance of initial and transition state structure of N—N bond cleaving. The difference is calculated as $\Delta d_{\mathrm{N-N}} = d^{\mathrm{TS}}_{\mathrm{N-N}} - d^{\mathrm{IS}}_{\mathrm{N-N}}$. All values are given in angstrom.

Surface	$d^{\mathrm{IS}}_{\mathrm{N-N}}$	$d^{\mathrm{TS}}_{\mathrm{N-N}}$	$\Delta d_{\mathrm{N-N}}$
Fe(110)	1.486	1.803	0.317
Co(0001)	1.479	1.929	0.450
Ni(111)	1.479	2.046	0.567
Cu(111)	1.470	1.951	0.481
Zn(0001)	1.457	2.113	0.656

Table 4.3: N—M bond distance (M = Fe, Co, Ni, Cu, or Zn) of adsorbed hydrazine in initial and transition state structure. The difference is calculated as $\Delta d_{\mathrm{N-M}} = d^{\mathrm{TS}}_{\mathrm{N-M}} - d^{\mathrm{IS}}_{\mathrm{N-M}}$. All values are given in angstrom.

Surface	$d^{\mathrm{IS}}_{\mathrm{N-M}}$	$d^{\mathrm{TS}}_{\mathrm{N-M}}$	$\Delta d_{\mathrm{N-M}}$
Fe(110)	2.137	1.992	-0.145
Co(0001)	2.081	1.909	-0.172
Ni(111)	2.026	1.873	-0.153
Cu(111)	2.108	1.961	-0.147
Zn(0001)	2.377	2.034	-0.343

from separate subsystems (the slab and molecule). E_{subs} is calculated as total energy difference between surface-only part of transition and initial geometry. E_{deform} is calculated similarly as E_{subs} for N_2H_4. $E^{\mathrm{TS}}_{\mathrm{A}}$ and $E^{\mathrm{TS}}_{\mathrm{B}}$ are the adsorption energies of fragment A and fragment B at the transition state. In the case of reaction $N_2H_4 \longrightarrow 2\,NH_2$, A and B are the two different NH_2 fragments. $E^{\mathrm{TS}}_{\mathrm{int}}$ is the interaction energy between A and B at transition state geometry. Finally, $E^{\mathrm{IS}}_{\mathrm{AB}}$ is the adsorption energy of hydrazine molecule at initial state geometry. Note that the adsorption energies $E^{\mathrm{TS}}_{\mathrm{A}}$ and $E^{\mathrm{TS}}_{\mathrm{B}}$ are calculated with respect to half of the total energy of gas phase hydrazine in *gauche* conformation.

Table 4.4: Activation energy decomposition analysis for $N_2H_4 \longrightarrow 2\,NH_2$. See text for the meaning of these terms.

Surface	E_{subs}	E_{deform}	E_{A}^{TS}	E_{B}^{TS}	$-E_{\text{AB}}^{\text{IS}}$	$-E_{\text{int}}^{\text{TS}}$	E_{act}
Fe(110)	0.01	0.68	-1.02	-1.02	1.28	0.30	0.23
Co(0001)	0.03	1.09	-0.82	-0.82	1.47	-0.56	0.39
Ni(111)	0.03	1.45	-0.62	-0.62	1.32	-1.07	0.49
Cu(111)	0.01	1.17	-0.51	-0.51	0.94	-0.51	0.59
Zn(0001)	0.14	1.69	0.30	0.30	0.29	-1.81	0.91

The result of the activation energy decomposition is given in Table 4.4. First, it is found that E_{subs} is relatively small (less than 0.05 eV) for all surfaces, except for Zn(0001). This means that the contribution of surface structure changes to the activation energy is relatively small. The largest value of E_{subs} is obtained for Zn(0001) which reflects the result that the geometrical change of this surface is more noticeable as compared to other surfaces (two Zn atoms which are bonded to NH_2 go upward as compared to their positions in initial geometry). E_{deform} is also found to be the largest for Zn(0001). The trend for this energy component is similar to the trend of $\Delta d_{\text{N-N}}$: the greater change in N—N bond length, the larger E_{deform} (see Table 4.2). The next energy contributions are adsorption energies E_{A}^{TS} and E_{B}^{TS}. Note that, because N—N bond cleaving process on the surfaces studied here is symmetric, E_{A}^{TS} and E_{B}^{TS} will have the same values. The trend of this component is similar to the trend of E_{act}. The stronger interaction between NH_2 with surface (the more negative value of E_{A}^{TS}) the lower activation barrier. Adsorption energy of hydrazine $E_{\text{AB}}^{\text{IS}}$ has opposite effect with E_{A}^{TS}. For similar adsorption energy at the transition state, the stronger interaction of hydrazine with surface (more negative $E_{\text{AB}}^{\text{IS}}$) the larger activation energy. This is found to be the case for Fe(110) and Co(0001) which are found to have similar E_{A}^{TS}. However, $E_{\text{AB}}^{\text{IS}}$ for Co(0001) is more negative which result in higher activation energy as compared to Fe(110). $E_{\text{int}}^{\text{TS}}$ mainly originate from the interaction of nitrogen atoms of different NH_2 fragments with surface. The largest value of $E_{\text{int}}^{\text{TS}}$ is obtained for Zn(0001) which may be taken as a sign for strong attractive interaction between N—N atoms of hydrazine.

4.2 Electronic structure aspects of N—N bond cleaving

To investigate electronic structure aspect of N—N bond cleaving of hydrazine we start by analyzing charge density difference ρ_{diff} of adsorbed hydrazine. This quantity is calculated as:

$$\rho_{\text{diff}} = \rho_{\text{mol/surf}} - \rho_{\text{mol}} - \rho_{\text{surf}} \tag{4.2}$$

where $\rho_{\text{mol/surf}}$ is the charge density of hydrazine adsorbed on surface, ρ_{mol} and ρ_{surf} denote charge density calculated separately with same atomic positions as found in adsorbed state for hydrazine and surface, respectively. Contour plots of ρ_{diff} of adsorbed hydrazine at initial and transition state geometry are shown in Figure 4.3. It can be observed that the charge density difference of adsorbed hydrazine has similar features for all surfaces considered here. Along the bond between N atom of hydrazine and surface atom negative charge difference (depletion) region is observed at both edges

(of N and surface atom) with positive charge difference (accumulation) region at the center of the bond. This positive charge difference is less pronounced on Cu(111) and Zn(0001) as compared to Fe(110), Co(0001), and Ni(111) which reflects the magnitude of hydrazine adsorption energy. Meanwhile, along the N—N bond at initial state, there is relatively small charge density difference which indicates that, in terms of charge density, the interaction between two N atoms in hydrazine is weaker than the interaction between the individual N atom and surface atom. However, at the transition state, there is substantial change in the charge density along N—N bond of hydrazine. Charge depletion region is observed at the center of N—N bond and accumulation region at both sides of the bond. The most pronounced charge accumulation around this area is observed for Zn(0001). This might be an indication that N—N interaction of hydrazine at transition state is the strongest on Zn(0001) as also have been hinted by the $E_{\text{int}}^{\text{TS}}$ term of Table 4.4.

To investigate the origin of N—N activation trend across the investigated surface, molecular orbitals (MOs) of adsorbed hydrazine will be investigated. Before considering the MOs of adsorbed hydrazine, it is useful first to consider MOs of hydrazine in gas phase for *cis* conformation with normal N—N bond length and the one with elongated N—N bond. This is useful for investigating change of MOs during N—N bond cleaving. The comparison of MOs for both structures is given in Figure 4.5. Hydrazine has 14 valence electrons which occupies 7 MOs. Figure 4.5 depicts the five highest occupied and two lowest unoccupied MOs along with their labels which will be used in this discussion. We have used the notation for diatomic molecules to label these molecular orbitals. Note that the $4\pi^*$ MO is the highest occupied molecular orbital (HOMO) while the 3π MO is second highest occupied molecular orbital (HOMO-1).

The change in the molecular orbitals of hydrazine during can be observed by plotting the molecular orbital energy levels as function of N—N bond length. In Figure 4.4 such plot is given. Visualization of molecular orbitals at the initial N—N bond and the elongated hydrazine is given in From Figures 4.4 and 4.5, it can be seen that MOs of hydrazine and elongated hydrazine structure are very similar. However, two differences can be observed. First, for elongated *cis* 5σ is higher in energy than 2π. Second, the unoccupied $6\sigma^*$ also lower in energy. It is now located just above the HOMO. So, at the transition state structure, the $6\sigma^*$ MO is the lowest unoccupied molecular orbital (LUMO). This pattern is also observed when N—N bond cleaving of hydrazine happens on metal surfaces.

In Figure 4.6 the electronic density of states (DOS) of initial and transition state projected to s, p_x, p_y, and p_z orbitals of nitrogen atom are shown. Zero energy levels for all plots are set to Fermi energy. At the initial state, three sharp peaks can be identified for all surfaces around the energy range of -12 to -8 eV. Within the geometry that is used in this work, N—N bond lies in x axis, 1π and $2\pi^*$ will be composed almost entirely of nitrogen p_y while 5σ of nitrogen p_z and p_x. Using this geometry, these three sharp peaks can be identified as derived orbitals (Kohn-Sham electronic states) from 1π, 5σ, and $2\pi^*$. These orbitals still retain their gas phase characteristics. At the transition state, these three peaks lie higher in energy with 5σ peak located higher than $2\pi^*$. This is similar to what was observed when comparing MOs of hydrazine and elongated hydrazine (see Figures 4.4 and 4.5). Peaks that are located higher in energy correspond to the derived orbitals due to interaction between HOMO-1 and HOMO with surface orbitals. These orbitals are dominated

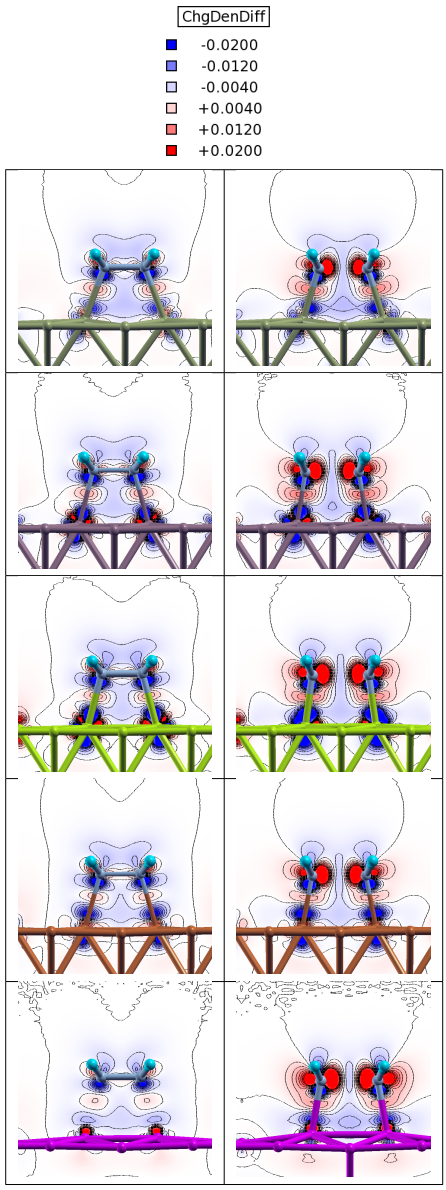

Figure 4.3: Contour plot of charge density difference of adsorbed hydrazine at initial (left) and transition geometry (right). From top to bottom: on Fe(110), Co(0001), Ni(111), Cu(111), and Zn(0001).

by contribution from p_z orbitals of nitrogen. At transition state, HOMO will be shifted to lower energy, while HOMO-1 will be shifted to higher energy.

The N—N bond cleaving process is mainly caused by the population of $6\sigma^*$-derived orbitals at transition state. These orbitals are dominated by nitrogen p_x and have N—N anti-bonding character. The interaction between gas phase $6\sigma^*$ MO of elongated hydrazine with surface d-orbitals (d-band) will result in bonding and anti-bonding orbitals with respect to surface atom in the case of sufficiently strong coupling between these orbitals. The $6\sigma^*$-derived bonding orbitals lie at lower energies and are readily occupied. Examples of such states are shown in the Figure 4.7. On Cu(111) and Zn(0001) the interaction between $6\sigma^*$ and d-orbitals due to large energy difference between them. However, the position of the peak of $6\sigma^*$-derived anti-bonding states vary as we go

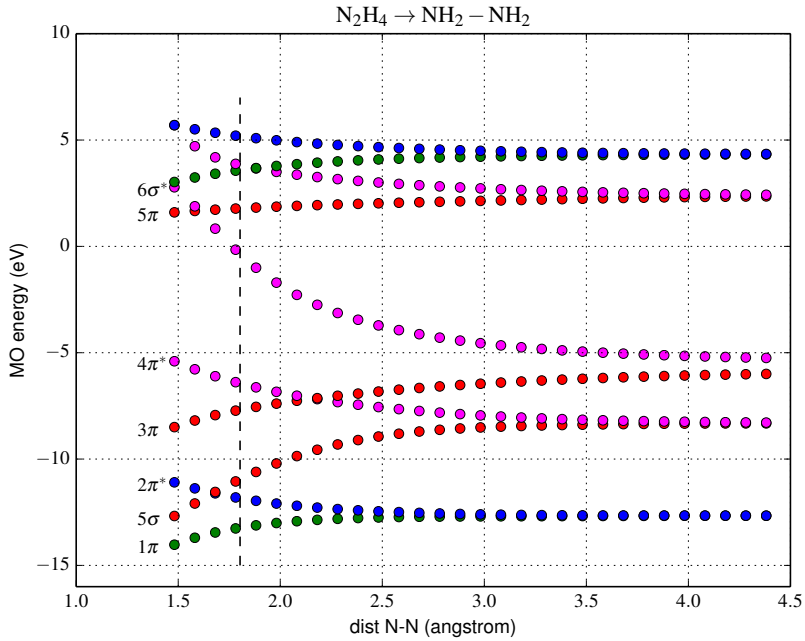

Figure 4.4: Molecular orbital energy levels of gas phase hydrazine as function of N—N bond length. Hydrazine is initially at the *cis* structure. A vertical dashed line corresponds to the N—N bond length of 1.8 Å, which is the shortest N—N bond length among the transition states found in this work (see Table 4.2). Vacuum energy is at 0 eV.

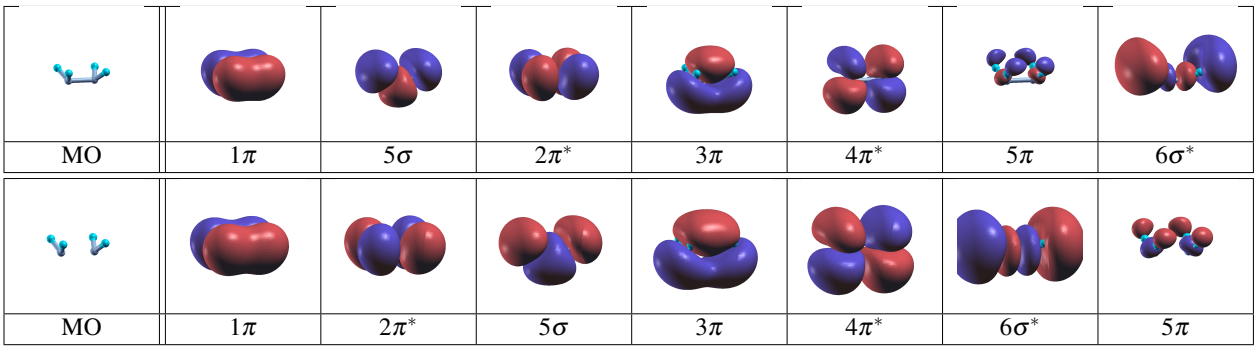

Figure 4.5: Gas phase molecular orbitals of hydrazine and hydrazine with elongated N—N bond ($d_{N-N} = 1.8$). These MOs are ordered according to their energy levels: from left to right energy level become higher. Highest occupied molecular orbital for both case is the $4\pi^*$ level.

from Fe(110) to Zn(0001). Examples of such states are shown in Figure 4.8. For Fe(110), peaks that correspond to $6\sigma^*$-derived anti-bonding states with surface atom lie above Fermi level. This results in stronger bonding between elongated hydrazine (transition state) with surface, thus more negative adsorption energy which will lead to lower activation energy. As we go down from Fe(110) to Zn(0001) these anti-bonding states lie lower in energy and are occupied by electrons. This will result in weaker interaction. Thus, from electronic structure perspective, the trend of activation energy for N—N bond cleaving on the surfaces that are considered here can be attributed to this occupation of $6\sigma^*$-derived orbitals.

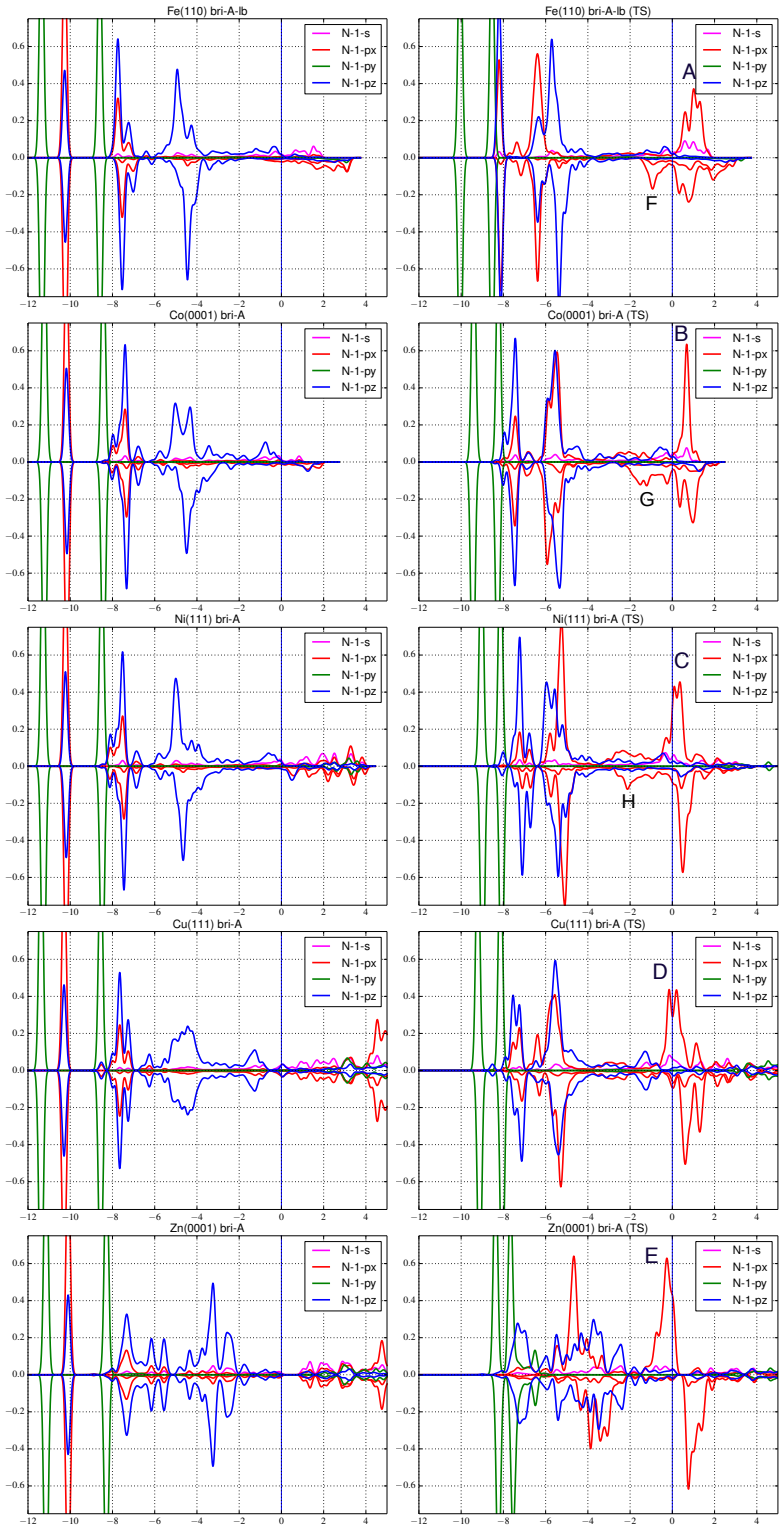

Figure 4.6: DOS projected on N atom of adsorbed hydrazine at initial (left) and transition geometry (right). Fermi level is at 0 eV. Several peaks related to $6\sigma^*$-derived orbitals at transition states have been marked by letters A–E. Visualization of such orbitals is given in Figure 4.8.

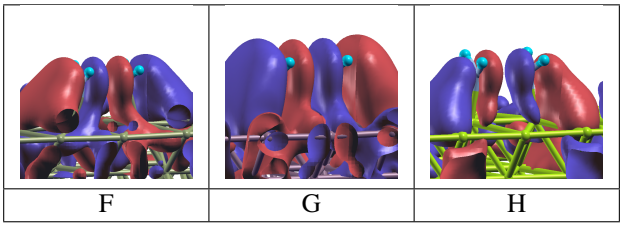

Figure 4.7: Visualization of Kohn-Sham orbitals which have $6\sigma^*$ character of elongated hydrazine on $3d$ surfaces, from left to right: Fe(110), Co(0001) and Ni(111). Aside from having N—N anti-bonding character, these orbitals also have bonding character with surface. The energy of these orbitals lie at the position indicated by letters F-H in Figure 4.6.

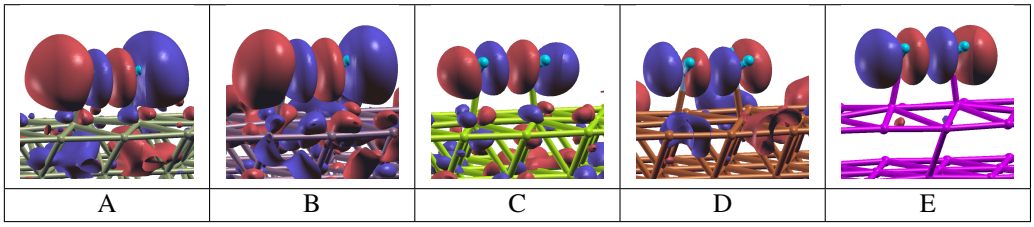

Figure 4.8: Visualization of Kohn-Sham orbitals which have $6\sigma^*$ character of elongated hydrazine on $3d$ surfaces, from left to right: Fe(110), Co(0001), Ni(111), Cu(111), and Zn(0001). Aside from having N—N anti-bonding character, these orbitals also have anti-bonding or non-bonding character with surface orbitals. As indicated by letters A-E in Figure 4.6, it can be seen that on Fe(110), Co(0001), and Ni(111) these orbitals are located above Fermi level while for Cu(111) and Zn(0001) they are located below Fermi level.

4.3 BEP relationship for N—N bond cleaving

We can extend our calculation to other surfaces. The result of the calculations are given in Table 4.5. For this data, we can see that N—N is generally an exothermic process on many surfaces except for Zn(0001), Pt(111), and Au(111).

From the data in Table 4.5 we can investigate interesting relation between various adsorption energies and activation energy. The so-called Brønsted-Evan-Polanyi (BEP) [67, 68] relationship is a linear relationship between activation energy E_{act} and reaction energy ΔE (see Table 4.1 for definition of ΔE). This relationship can written as

$$E_{\text{act}} = m\Delta E + b \tag{4.3}$$

where m and b are some constants. Using density functional calculations it has been shown that this relationship holds for several elementary reaction steps [69–75]. By knowing this relationship for a type of reaction, the corresponding activation energies can be estimated from the information of ΔE alone. This allows us to quickly screen various model catalysts suitable for certain reactions. Recently, generalization of BEP relationship has been proposed [76] to include other energetic parameters or descriptors other than ΔE.

Although BEP relationship has been found to hold for N—N bond cleaving by several previous studies, to our knowledge the BEP relationship for N—N bond cleaving of hydrazine is not yet

Table 4.5: Energetics of N—N bond cleaving on various metal surfaces. (see Table 4.1 for definition of various terms.)

Surface	E_{ini}	E_{fin}	ΔE	E_{act}
Sc(0001)	-1.46	-5.26	-3.80	0.09
Ti(0001)	-1.71	-5.39	-3.68	0.08
V(110)	-1.80	-5.02	-3.22	0.15
Cr(110)	-1.73	-4.22	-2.49	0.23
Fe(110)	-1.28	-3.24	-1.96	0.23
Co(0001)	-1.47	-2.83	-1.36	0.39
Ni(111)	-1.32	-2.35	-1.04	0.49
Cu(111)	-0.94	-2.03	-1.09	0.59
Zn(0001)	-0.29	+0.42	+0.71	0.91
Y(0001)	-1.36	-5.13	-3.77	0.11
Zr(0001)	-1.66	-5.01	-3.34	0.14
Nb(110)	-1.73	-4.79	-3.06	0.19
Mo(110)	-1.72	-2.99	-1.27	0.22
Ru(0001)	-2.01	-3.29	-1.28	0.45
Rh(111)	-1.75	-2.69	-0.93	0.44
Pd(111)	-1.34	-1.84	-0.51	0.90
Ag(111)	-0.55	-1.03	-0.47	1.10
Cd(0001)	-0.25	-0.33	-0.09	1.20
La(0001)	-1.33	-4.77	-3.44	0.21
Hf(0001)	-2.40	-5.93	-3.53	0.10
Ta(110)	-2.18	-4.13	-1.94	0.13
W(110)	-2.05	-3.38	-1.33	0.22
Re(0001)	-2.24	-3.18	-0.94	0.26
Os(0001)	-2.50	-3.09	-0.59	0.30
Ir(111)	-2.20	-2.28	-0.08	0.26
Pt(111)	-2.13	-1.95	+0.18	0.46
Au(111)	-1.06	+0.03	+1.08	1.17

published before. Here, we investigate three descriptors for estimating activation energy of N—N bond cleaving of hydrazine, namely the reaction energy ΔE, adsorption energy of N_2H_4, and adsorption energy of $2\,NH_2$. The relationship between these descriptors and activation energies of N—N bond cleaving on several metal surfaces are shown in Figures 4.9, 4.10, and 4.11.

The relation between activation E_{act} and reaction energy ΔE is given in Figure 4.9. This is the usual BEP relationship. The equation of the BEP line is $E_{\text{act}} = 0.18\Delta E + 0.70$. The R^2-value [1] is about 0.76 which is relatively good (compared to that for O—H bond cleaving which have R^2-value about 0.61 [76]). Closer inspection to the plot might suggest that better R^2-value might be obtained if we only consider subset of surfaces, for example by including only $3d$ metal surfaces.

Because the transition state of N—N bond cleaving of hydrazine closely resembles the initial state, one might wonder whether the adsorption energy of hydrazine E_{ini} can be used as descriptor for estimating the activation energy. We plot the relation between the activation and adsorption energy in Figure 4.10. The equation of the BEP line is given by $E_{\text{act}} = 0.42E_{\text{ads}(N_2H_4)} + 1.06$. The

[1] The closer R^2-value to 1 the better the linear relationship.

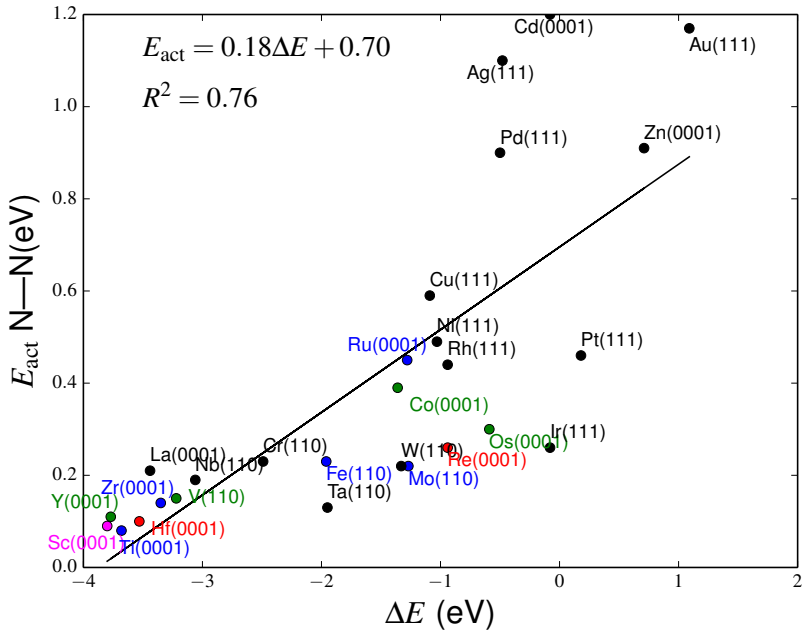

Figure 4.9: BEP relationship between activation E_{act} and reaction energy ΔE. In this figure and the following, we have used different color to help differentiating between close data points.

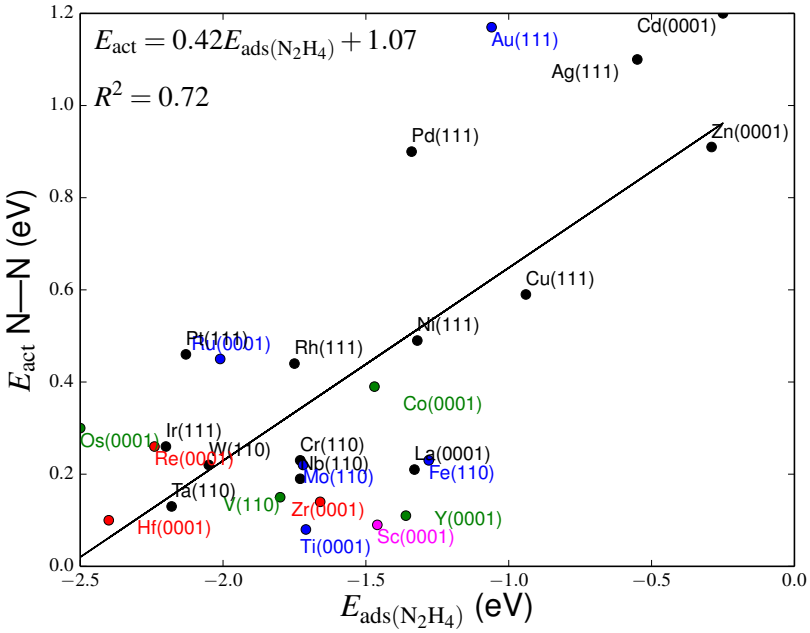

Figure 4.10: BEP relationship between activation E_{act} and adsorption energy of N_2H_4.

obtained R^2-value is lower than that obtained for Figure 4.9 which suggest that this descriptor is less suitable than ΔE. However, this descriptor still can be useful for certain surfaces, for example Pd(111), Ag(111), and Cd(0001).

The third descriptor that we investigate is the adsorption energy of the product of the reaction, namely the adsorption energy of $2\,NH_2$. The BEP relationship is plotted in Figure 4.11. The equation of the BEP line is given by $E_{act} = 0.18E_{ads(2\,NH_2)} + 0.98$. The obtained R^2-value is about 0.89 which is the highest among the three descriptors that are considered. This result is similar

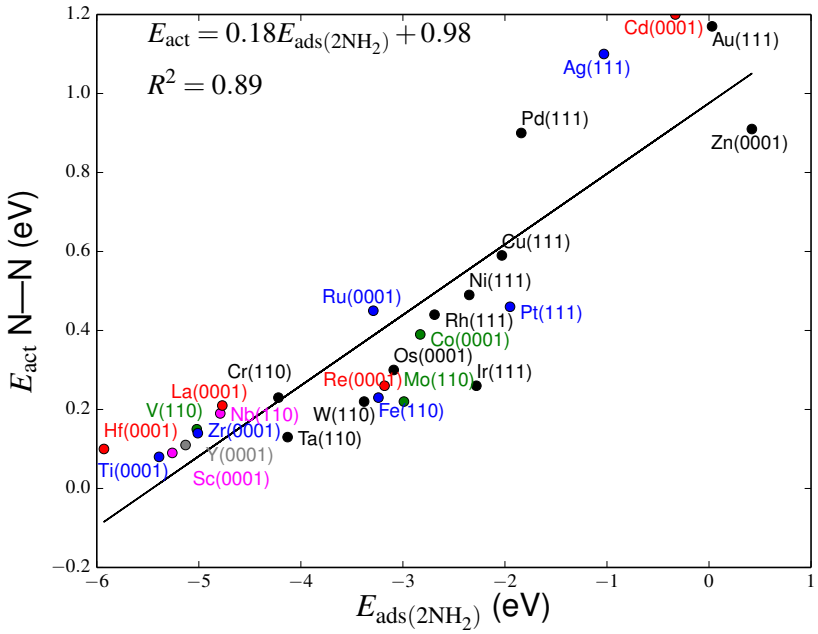

Figure 4.11: BEP relationship between activation E_{act} and adsorption energy of $2\,NH_2$.

to that found for O—H bond cleaving [76] which suggest that adsorption energy of dissociation products to be a good descriptor for estimating activation energy.

4.4 Chapter summary

Here, we give a list of important findings in this chapter.

- The activation energy of the N—N bond cleaving of hydrazine are found to have values in the range 0.08–1.20 eV across different surfaces that we investigated. N—N bond cleaving of hydrazine generally is found to be an exothermic process, except for Zn(0001), Pt(111), and Au(111).
- For 3*d* metal surfaces, going from Fe(110) to Zn(0001) the N—N activation energy is found to have increasing trend. This trend is related to the occupation of LUMO-derived orbitals of hydrazine at the transition state.
- The BEP relationship is found to hold for the N—N bond cleaving. Three descriptors have been investigated for estimating activation energy of N—N bond cleaving: ΔE, $E_{ads(N_2H_4)}$, and $E_{ads(2\,NH_2)}$. Adsorption energy of $2\,NH_2$ is found to be the most suitable descriptor among them.

In this chapter, we have presented a systematic study of N—N bond cleaving on several 3*d* metal surfaces which is not yet available in the literature. The approach taken in this study can also be applied to other surfaces. BEP relationship (and its extension) for N—N bond cleaving of hydrazine is established for the first time in this study.

CHAPTER 5

First N—H bond cleaving of hydrazine

In the previous chapter we have discussed about N—N bond cleaving of hydrazine. In this chapter we discuss another possible first step of hydrazine decomposition reaction, namely the N—H bond cleaving. Further N—H bond cleaving, i.e. N—H bond cleaving of N_2H_3, N_2H_2, and N_2H will be discussed in the next chapter. In this work, we will also refer to N—H bond cleaving of N_2H_4 as the *first* N—H bond cleaving of hydrazine, N—H bond cleaving of N_2H_3 as second N—H bond cleaving, etc. All of these N—H bond cleaving processes will also be referred to as dehydrogenation. We will follow a similar approach as we have done for N—N bond cleaving in the previous chapter.

5.1 Energetics of the first N—H bond cleaving

Geometries of the initial, transition, and final state of the first N—H bond cleaving is given in Figure 5.1. Note that we have used the hydrazine adsorbed in *bri-B* configuration as the initial state. From Figure 5.1, it is found that the transition state have roughly similar structures. Slightly different transition state structure is obtained on Fe(110) where the NH fragment of N_2H_3 is adsorbed in short bridge site instead of top site as found on other surfaces. At final state the broken H atom of hydrazine is adsorbed on the hollow site and the remaining N_2H_3 is adsorbed on hollow site, except for Zn(0001). For Zn(0001), N_2H_3 is adsorbed on bridge site. Similar transition state geometries are also observed in previous studies of first N—H bond cleaving of hydrazine on Ir(111) [41] and Rh(111) [42].

The energetics of first N—H bond cleaving of hydrazine can be found in Table 5.1. The imaginary frequencies corresponding to N—H bond stretch at the transition state are also given in Table 5.1. The visualization of these energetics is given in Figure 5.2. For all surfaces, except Zn(0001), the first N—H bond cleaving are calculated to be an exothermic process. The exothermicity is reduced as we go from Fe(110) to Zn(0001). More importantly, the activation energy for first N—H bond cleaving of hydrazine is increasing as we go from Fe(110) to Zn(0001). Comparison of the values of E_{act} of N—H with that of N—N (Table 4.1) shows that the first N—H bond cleaving on the same surface has higher activation energy and thus is more difficult to happen than N—N bond cleaving.

Two geometry quantities, the distance between N—H of the broken bond $d_{\text{N}-\text{H}}$ and the distance between N atom of the broken bond and surface atom $d_{\text{N}-\text{M}}$ (M = Fe, Co, Ni, Cu, or Zn), are given in Table 5.2 and 5.3, respectively for initial and transition state. From Table 5.2 it can be seen that from Fe(110) to Zn(0001), the distance $d^{\text{IS}}_{\text{N}-\text{H}}$ has slightly decreasing trend. At transition

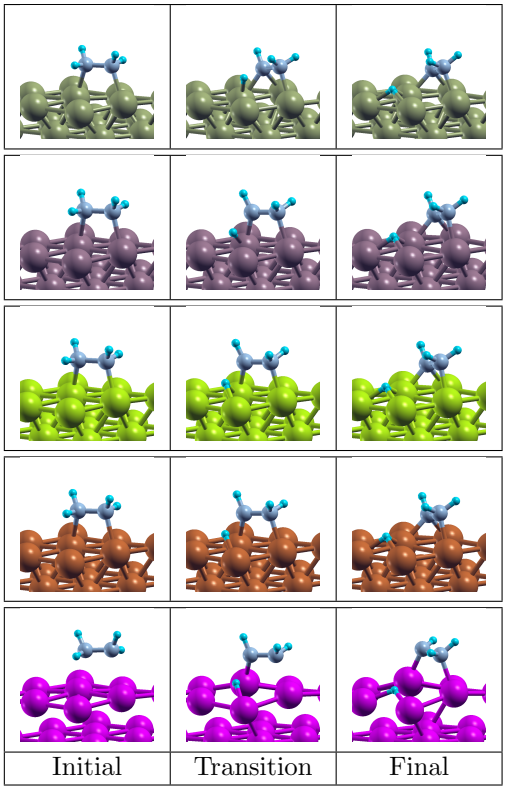

Figure 5.1: Initial, transition, and final state geometries for the first N—H bond cleaving of hydrazine on Fe(110), Co(0001), Ni(111), Cu(111), and Zn(0001).

Table 5.1: Calculated adsorption energies of initial E_{ini}, transition E_{TS}, and final structure E_{fin} of first N—H bond cleaving of hydrazine. ΔE is calculated as $E_{\mathrm{fin}} - E_{\mathrm{ini}}$. All energies are given in eV and calculated relative to gas phase hydrazine in gauche conformation. The imaginary frequecies are given in cm^{-1}.

Surface	E_{ini}	E_{TS}	E_{fin}	ΔE	E_{act}	ν^{TS}
Fe(110)	-1.34	-0.86	-2.28	-0.94	0.48	1146.5i
Co(0001)	-1.50	-0.62	-2.04	-0.54	0.88	1110.5i
Ni(111)	-1.35	-0.43	-1.69	-0.34	0.92	978.0i
Cu(111)	-1.03	0.12	-1.14	-0.10	1.15	1016.8i
Zn(0001)	-0.54	1.14	0.86	1.40	1.68	620.6i

state, however, the distance $d^{\mathrm{TS}}_{\mathrm{N-H}}$ has increasing trend from Fe(110) to Zn(0001). The change of the distance $\Delta d_{\mathrm{N-H}}$ has increasing trend from Fe(110) and Zn(0001). All of these trends suggest that N—H bond of hydrazine becomes stronger as we go from Fe(110) to Zn(0001).

Meanwhile, from Table 5.3, it can be seen that the distance $d^{\mathrm{IS}}_{\mathrm{N-M}}$ does not show a clear trend from Fe(110) to Zn(0001). The minimum and maximum of $d^{\mathrm{IS}}_{\mathrm{N-M}}$ are found on Ni(111) and Zn(0001), respectively. The minimum of $d^{\mathrm{TS}}_{\mathrm{N-M}}$ is also found on Ni(111). However, the maximum of $d^{\mathrm{TS}}_{\mathrm{N-M}}$ is found on Fe(110) instead, because at the transition state the N_2H_3 fragment is already adsorbed on hollow site, while on other surfaces the N_2H_3 fragment is still adsorbed on the bridge site. For all surfaces, the change of distance $\Delta d_{\mathrm{N-M}}$ is found to to be negative. This might be interpreted as smaller repulsion between surface and N_2H_3 as compared to N_2H_4.

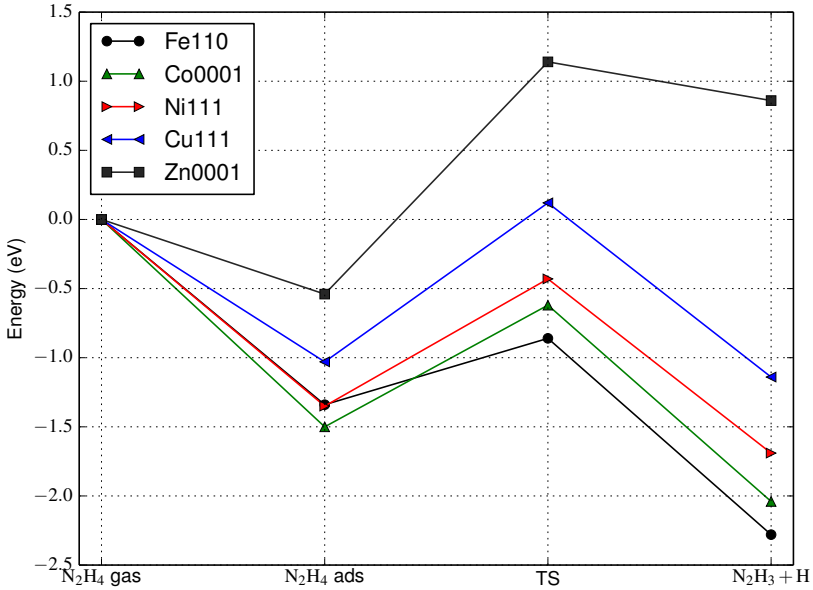

Figure 5.2: Energy diagram for N—H bond cleaving of hydrazine. The energies are calculated relative to sum of energies of isolated slab and gas phase hydrazine in *gauche* conformation.

Table 5.2: N—H bond distance of adsorbed hydrazine in initial and transition state structure of the first N—H bond cleaving. The difference is calculated as $\Delta d_{\mathrm{N-H}} = d^{\mathrm{TS}}_{\mathrm{N-H}} - d^{\mathrm{IS}}_{\mathrm{N-H}}$. All values are given in angstrom.

Surface	$d^{\mathrm{IS}}_{\mathrm{N-H}}$	$d^{\mathrm{TS}}_{\mathrm{N-H}}$	$\Delta d_{\mathrm{N-H}}$
Fe(110)	1.030	1.346	0.316
Co(0001)	1.029	1.530	0.501
Ni(111)	1.029	1.576	0.547
Cu(111)	1.028	1.648	0.620
Zn(0001)	1.023	1.803	0.780

Table 5.3: N—M bond distance (M = Fe, Co, Ni, Cu, or Zn) of adsorbed hydrazine in initial and transition state structure of the first N—H bond cleaving. The difference is calculated as $\Delta d_{\mathrm{N-M}} = d^{\mathrm{TS}}_{\mathrm{N-M}} - d^{\mathrm{IS}}_{\mathrm{N-M}}$. All values are given in angstrom.

Surface	$d^{\mathrm{IS}}_{\mathrm{N-M}}$	$d^{\mathrm{TS}}_{\mathrm{N-M}}$	$\Delta d_{\mathrm{N-M}}$
Fe(110)	2.165	2.157	-0.008
Co(0001)	2.108	1.952	-0.156
Ni(111)	2.062	1.928	-0.134
Cu(111)	2.163	1.978	-0.185
Zn(0001)	2.503	2.026	-0.477

In order to find more insights into the first N—H bond cleaving of hydrazine we also did activation energy decomposition analysis according to the Equation 4.1 introduced in the previous chapter. The result of the activation energy decomposition for the first N—H bond cleaving of hydrazine is summarized in Table 5.4. Note that for this case, AB is the N_2H_4 molecule, A fragment is taken to be the N_2H_3 and B fragment is taken to be the H atom. First, we note that E_{subs} is relatively small, except for Zn(0001). This means that except for Zn(0001), change in surface structure does not contribute much to the activation energy. A similar result is also obtained for

N—N bond cleaving in the previous chapter. The deformation energy cost of hydrazine from initial to transition state E_{deform} is found to have increasing trend from Fe(110) to Zn(0001). This trend is consistent with the trend of $\Delta d_{\text{N-H}}$ which is also becomes larger from Fe(110) to Zn(0001) (see Table 5.2). The adsorption energy of N_2H_3 at the transition state, i.e. E_{A}^{TS} is found to be less exothermic from Fe(110) to Zn(0001). However, the trend of H atom adsorption at the transition state, i.e. E_{B}^{TS} is not obvious. The lowest value of E_{B}^{TS} is found to be on Ni(111) while the highest is found on Zn(0001). For all surfaces, except on Zn(0001), the magnitude of E_{A}^{TS} is larger than E_{B}^{TS} so it can be said that the interaction of N_2H_3 fragment with surface has more effect to the first N—H bond activation energy as compared to the interaction of H atom with surface. The magnitude of $E_{\text{int}}^{\text{TS}}$ becomes larger as we go from Fe(110) to Zn(0001). Similar with the previous analysis on N—N bond cleaving, large magnitude of $E_{\text{int}}^{\text{TS}}$ may be taken as sign of strong N—H attractive interaction.

Table 5.4: Activation energy decomposition analysis for $N_2H_4 \longrightarrow N_2H_3 + H$.

Surface	E_{subs}	E_{deform}	E_{A}^{TS}	E_{B}^{TS}	$-E_{\text{AB}}^{\text{IS}}$	$-E_{\text{int}}^{\text{TS}}$	E_{act}
Fe(110)	-0.02	1.17	-1.30	-0.16	1.34	-0.55	0.48
Co(0001)	-0.01	2.02	-0.72	-0.39	1.50	-1.53	0.88
Ni(111)	0.00	2.24	-0.46	-0.36	1.35	-1.85	0.92
Cu(111)	0.03	2.81	-0.23	-0.18	1.03	-2.32	1.15
Zn(0001)	0.38	3.77	0.68	1.10	0.54	-4.79	1.68

5.2 Electronic structure aspects of first N—H bond cleaving

Analyzing the electronic structure change of the first N—H bond cleaving of hydrazine is not as straightforward as that of the N—N bond cleaving. It is difficult to visualize the change in the electronic structure of hydrazine at as N—H broke in the gas phase because it involves more than just N—H bond stretching. However, we still can do some analysis if we consider only the hydrazine molecule part of the transition state (excluding the surface). The transition state structures are roughly similar on the different metal surfaces. In Figure 5.3 five valence MOs plus LUMO of hydrazine as found in the transition state of N—H bond cleaving are visualized. We can see that these orbitals do not have similarities with any of MOs of hydrazine in *anti*, *cis*, and *gauche* conformations. The most important of these MOs are the HOMO (MO7) and LUMO (MO8). The HOMO of this structure does not have contribution from the broken H atom. The HOMO will be responsible to the bonding character of N_2H_3 with surface. Meanwhile, the LUMO has N—H anti-bonding character by noticing the existence of node between the one H atom with nitrogen. Upon the interaction with surface this LUMO will interact with surface orbitals. Recall that, for N—N bond cleaving the LUMO of the transition state, i.e. the $6\sigma^*$ MO, which has the N—N anti-bonding character, is also responsible for the trend of N—N activation energy. We also expect that the LUMO of the transition state for N—H bond cleaving will also be responsible for the trend of N—H activation energy.

To analyze the electronic structure of hydrazine at the transition state of first N—H bond cleaving, we found that it is more convenient to use MO-projected DOS rather that atomic-projected

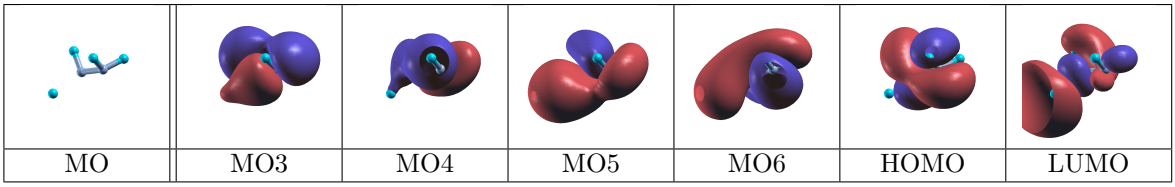

Figure 5.3: Molecular orbitals of the transition state of N—H bond cleaving of hydrazine

DOS. Projected DOS on HOMO and LUMO of the transition states for first N—H bond cleaving of hydrazine can be found in Figure 5.4. We also provide the DOS projected on the broken hydogen and nitrogen atom of hydrazine in Figure 5.4.

On Figure 5.4 we have labeled several peaks of LUMO-projected DOS. We can see similar pattern as we have seen for N—N bond cleaving in the previous chapter. The interaction of LUMO with *d*-band of surfaces will give rise to bonding and anti-bonding orbital if these interaction are strong. Such bonding orbitals are found for the case of Fe(110), Co(0001), and Ni(111) and have been labeled by letters F–H. The visualization of them can be found in Figure 5.6. These orbitals are readily occupied. This will result in lower energy of transition states thus lowering the activation energies. Meanwhile, the occupation of anti-bonding or non-bonding orbitals can result in higher energy of the transition states and thus high activation energies. Examples of these anti-bonding orbitals are shown in Figure 5.5. The position of these anti-bonding peaks are lower in energy as we go from Fe(110) to Zn(0001).

5.3 BEP relationship for first N—H bond cleaving

We can extend our calculations of first N—H bond cleaving activation energies to other surfaces. The result of the calculations are given in Table 5.5. From Table 5.5 we can see that for most surfaces the first N—H bond cleaving is exothermic, except on Zn(0001), Rh(111), Pd(111), and Pt(111). By comparison with N—N bond cleaving we see that first N—H bond cleaving generally has smaller reaction energy and less exothermic. More importantly, the activation energy of N—H bond cleaving is found to be higher than the N—N bond cleaving for most surfaces.

Similarly with the N—N bond cleaving, we also can establish the BEP relationship for the first N—H bond cleaving of hydrazine. Here, we investigate three descriptors for estimating activation energy of first N—H bond cleaving, namely the reaction energy ΔE, adsorption energy of initial state $E_{\mathrm{ads}(N_2H_4)}$, and adsorption energy of final state $E_{\mathrm{ads}(N_2H_3+H)}$.

In Figure 5.7 we plot the relationship between E_{act} and ΔE. The R^2-value of 0.79 suggests that ΔE is a good descriptor for estimating activation energy of N—H bond cleaving. In Figure 5.8 we plot the relationship between E_{act} and $E_{\mathrm{ads}(N_2H_4)}$. The obtained R^2-value suggests that this descriptor is less suitable than ΔE. Finally, in Figure 5.8 the relationship between E_{act} and $E_{\mathrm{ads}(N_2H_3+H)}$ is plotted. The obtained R^2-value suggests that this descriptor is the most suitable among the three descriptors that we consider. This is similar to the result that we obtained for N—N bond cleaving in the previous chapter and previous results for O—H bond cleaving [76].

Table 5.5: Energetics of N—H bond cleaving on various metal surfaces.

Surface	E_{ini}	E_{fin}	ΔE	E_{act}
Fe(110)	-1.34	-2.28	-0.94	0.48
Co(0001)	-1.50	-2.04	-0.54	0.88
Ni(111)	-1.35	-1.69	-0.34	0.92
Cu(111)	-1.03	-1.15	-0.10	1.15
Zn(0001)	-0.54	+0.86	+1.40	1.68
Ru(0001)	-2.02	-2.44	-0.42	0.90
Rh(111)	-1.77	-1.64	+0.13	0.86
Pd(111)	-1.38	-1.20	+0.18	0.96
Os(0001)	-2.51	-3.10	-0.59	0.77
Ir(111)	-2.20	-2.21	-0.01	0.67
Pt(111)	-2.15	-1.96	+0.19	0.69
Mo(110)	-2.00	-3.46	-1.46	0.55
Nb(110)	-1.83	-3.59	-1.76	0.56
W(110)	-2.08	-3.78	-1.70	0.65

5.4 Chapter summary

Here, we give a list of important findings in this chapter.

- The activation energies of the N—H bond cleaving of hydrazine are found to have values in the range 0.48–1.68 eV across different metal surfaces that we consider here. N—H bond cleaving of hydrazine generally is found to be an exothermic process, except for Zn(0001), Rh(111), Pd(111), and Pt(111). Compared to N—N bond cleaving, the reaction energy of N—H bond cleaving is smaller.

- For 3*d* metal surfaces, going from Fe(110) to Zn(0001) the N—H activation energy is found to have increasing trend. This trend is similar to the trend of N—N activation energy. This trend is also related to the occupation of LUMO-derived orbitals of hydrazine at the transition state.

- On the same surface, the activation energy of N—H bond cleaving is found to be larger than the activation energy of N—N bond cleaving.

- Similar with the N—N bond cleaving, the BEP relationship is found to hold for the N—H bond cleaving. Three descriptors have been investigated for estimating activation energy of N—H bond cleaving: ΔE, $E_{\text{ads}(N_2H_4)}$, and $E_{\text{ads}(N_2H_3+H)}$. The adsorption energy of $N_2H_3 + H$ is found to be the most suitable descriptor among them.

Together with the results of the previous chapter, it is found that N—N bond cleaving is more preferable than N—H bond cleaving on the metal surfaces that we investigated. The transition state for N—N bond cleaving can already be reached by simple N—N bond stretching. Meanwhile, for N—H bond cleaving, to reach the transition state NH_2 part of hydrazine needs to rotate towards the surface. This rotation can then be followed by N—H bond stretching. A more complex geometrical

change required to reach the transition state of N—H as compared to N—N bond cleaving might be responsible for higher activation energy of N—H bond cleaving. The N—N bond cleaving is suggested to be responsible for the presence of adsorbed NH_2 which is reported in many experimental studies. BEP relationship (and its extension) for N—H bond cleaving of hydrazine is also established for the first time in this study.

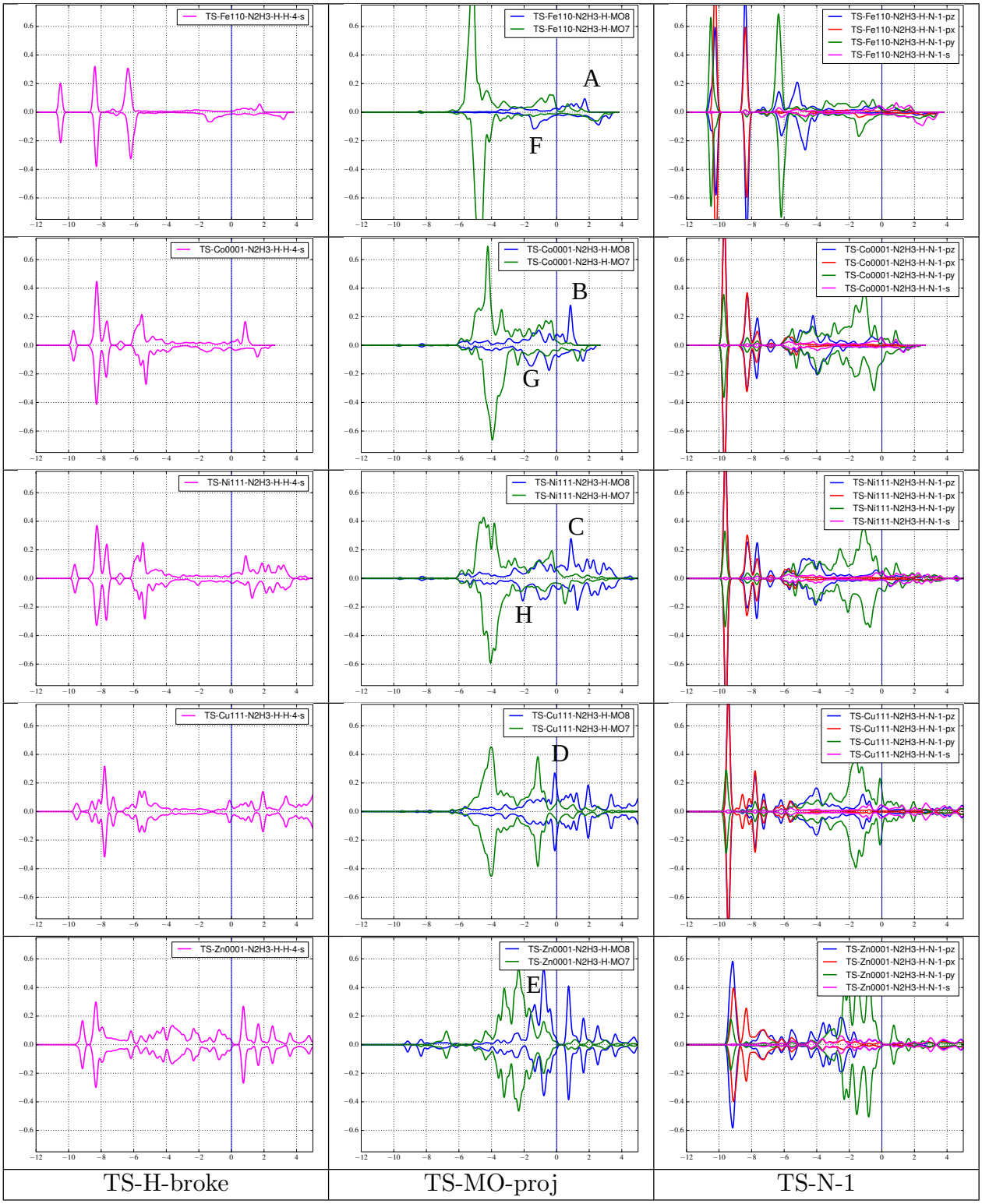

Figure 5.4: Various DOS of the transition state for first N—H bond cleaving of hydrazine. The Fermi level is at 0 eV. The first column gives DOS projected on the broken H atom of hydrazine. The second column gives DOS projected on HOMO and LUMO of hydrazine at the transition state. The third column gives DOS projected on the N atom of hydrazine where the N—H bond is broken. Visualization of the orbitals corresponding to the letters A–E and F–G can be found in Figures 5.5 and 5.6 respectively

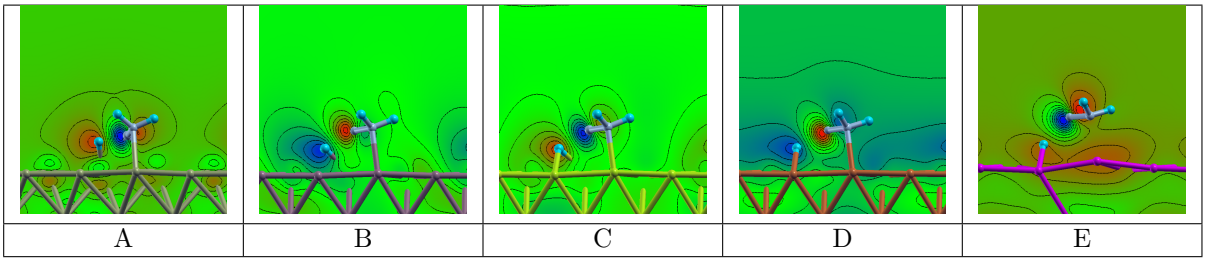

Figure 5.5: Visualization of the orbitals associated with the letters A–E given in Figure 5.4. These orbitals have N—H anti-bonding character. These orbitals also have non-bonding or anti-bonding characters with surface. For Fe(110), Co(0001), and Ni(111) these orbitals are located above the Fermi level while for Cu(111) and Zn(0001) they are below the Fermi level.

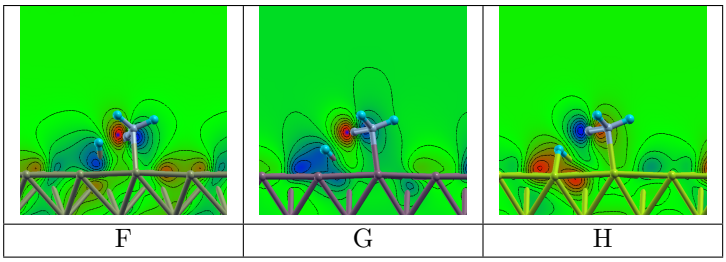

Figure 5.6: Visualization of the orbitals associated with the letters F–H given in Figure 5.4. These orbitals have N—H anti-bonding character. These orbitals also have bonding characters with surface. These orbitals are found only for surfaces which have considerable interaction with LUMO of the transition state such as Fe(110), Co(0001), and Ni(111).

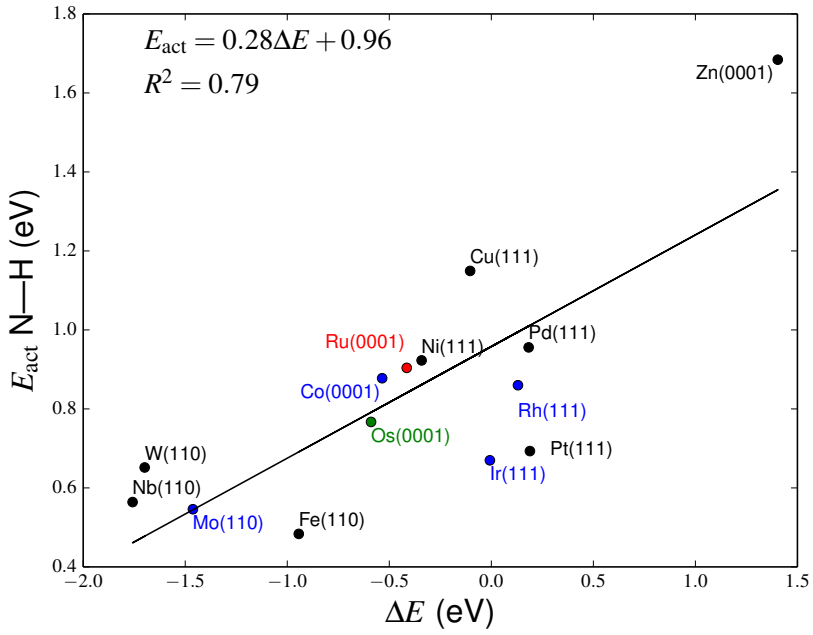

Figure 5.7:]
BEP relationship between activation E_{act} and reaction energy ΔE

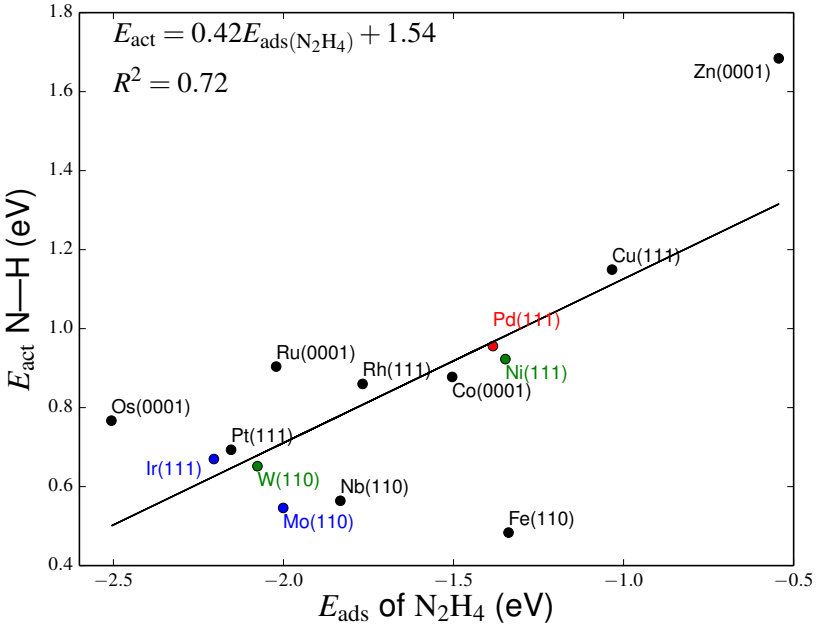

Figure 5.8: BEP relationship between activation E_{act} and adsorption energy of N_2H_4

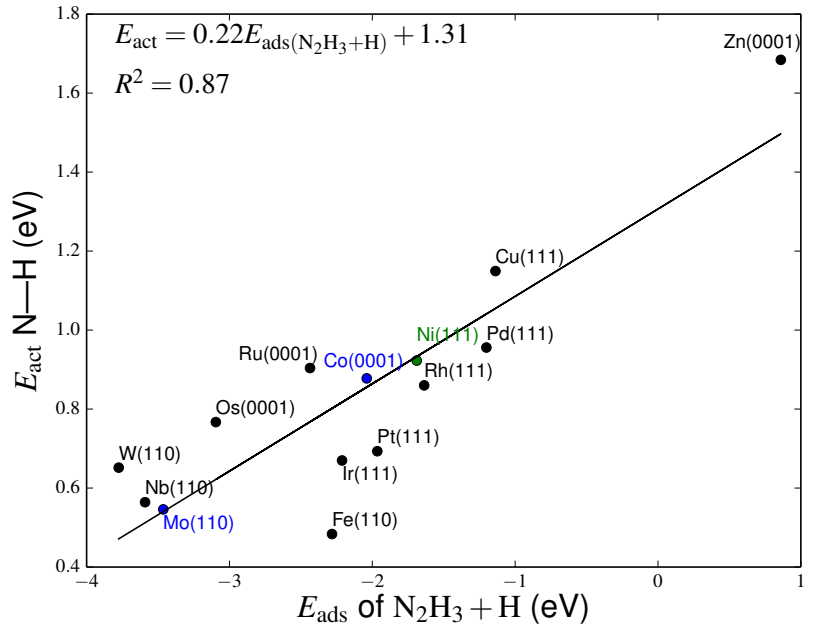

Figure 5.9: BEP relationship between activation E_{act} and adsorption energy of $N_2H_3 + H$

CHAPTER 6

Reaction pathways of hydrazine dehydrogenation on Ni(111) surface

In the previous chapter, we have discussed about the first N—H bond cleaving of hydrazine. In this chapter, we consider the subsequent N—H bonds cleaving processes of hydrazine or the dehydrogenation reactions. The dehydrogenation of hydrazine may be thought of as a subreaction of the decomposition reaction. We focus our attention on Ni(111) because Ni-based catalyst is being investigated as anode catalyst in direct hydrazine fuel cell [3,77]. From the experiments, it is found that preventing decomposition of hydrazine is important to obtain good performance of the fuel cell. We will consider two possible pathways for hydrazine decomposition namely the direct dehydrogenation and NH_2-assisted dehydrogenation. In direct dehydrogenation, the N—H bond of hydrazine is cleaved directly without presence of any coadsorbates and the broken H atom is adsorbed on the surface. In NH_2-assisted dehydrogenation, the N—H bond of hydrazine is cleaved by H atom transfer to nearby NH_2 coadsorbate. Because the product of NH_2-assisted dehydrogenation is ammonia (NH_3), we will also refer to this step as ammonia formation. Several previous computational studies of hydrazine decomposition reaction pathways have been done for Ir(111) [41], Fe(211) [40], Rh(111) [41], and Ir clusters [78].

6.1 Direct dehydrogenation of hydrazine

A list of considered reaction steps for direct dehydrogenation of hydrazine and their activation energies are summarized in Table 6.1. The relative energies for the initial, transition, and final states of these reaction steps are shown in Figure 6.1. We note that the activation energies of direct dehydrogenation are relatively similar between first, second, and third dehydrogenation steps, namely about 1.00 eV. The last dehydrogenation step is found to have the lowest activation energy.

6.1.1 First dehydrogenation

We calculate two possibilities for this step, namely the reaction steps RS-1 and RS-2. The initial, transition, and final states of these reaction steps are shown in Figure 6.2. In the reaction steps RS-1 and RS-2, one NH_2 group of hydrazine will rotate towards the surface. This rotation will be followed by N—H bond breaking. At the final state, one hydrogen atom will be adsorbed on the surface. The hydrogen atom will be adsorbed on the fcc hollow site for RS-1 and hcp hollow site for

Table 6.1: List of the considered reaction steps for direct dehydrogenation of hydrazine.

Reaction step	E_{act} (eV)
RS-1: $N_2H_4 \longrightarrow N_2H_3 + H$	0.92
RS-2: $N_2H_4 \longrightarrow N_2H_3 + H$	0.92
RS-3: $N_2H_3 \longrightarrow N_2H_2 + H$	1.00
RS-4: $N_2H_3 \longrightarrow N_2H_2 + H$	1.27
RS-5: $N_2H_2 \longrightarrow N_2H + H$	0.99
RS-6: $N_2H_2 \longrightarrow N_2H + H$	1.00
RS-7: $N_2H_2 \longrightarrow N_2H + H$	1.00
RS-8: $N_2H \longrightarrow N_2 + H$	0.72

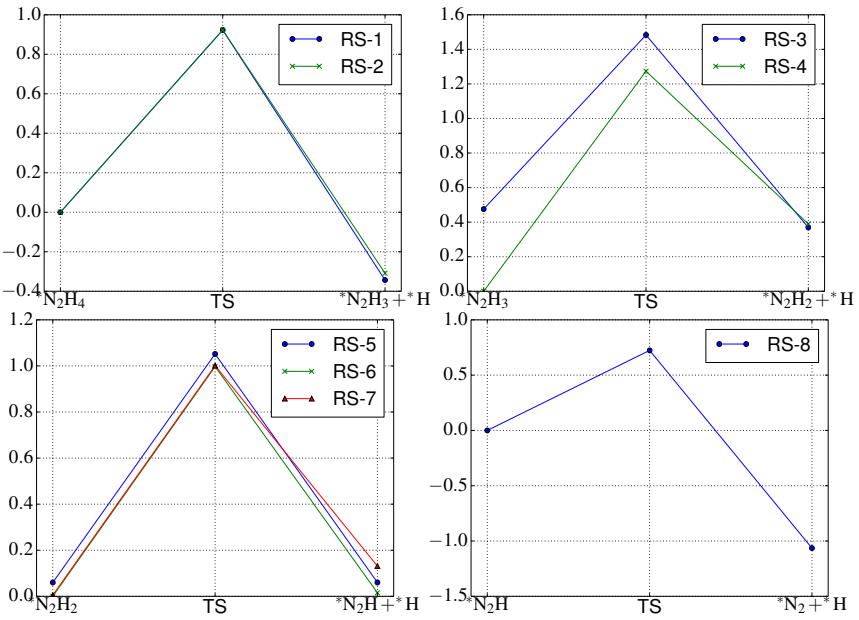

Figure 6.1: Relative energies among the dehydrogenation reaction steps. The energy of the most stable structure for each step is shifted to 0 eV.

RS-2. At final state, the remaining N_2H_3 will move from bridge site to hollow site. Even though the final states are the different, the calculated activation energies for these reaction steps are similar, i.e. 0.92 eV.

6.1.2 Second dehydrogenation

Two possibilities are considered here, namely the reaction steps RS-3 and RS-4. The initial, transition, and final states of these reaction steps are shown in Figure 6.3. For RS-3, the initial state is the N_2H_3 fragment adsorbed on the bridge site. This structure has higher energy as compared to adsorption in hollow site. The dehydrogenation process is also initiated by rotation of NH_2 fragment followed with N—H bond breaking. In the final state, the broken hydrogen atom is adsorbed in hcp hollow site and the remaining N_2H_2 becomes adsorbed on another hcp hollow site. Alternative second dehydrogenation is the reaction step RS-4. The initial state for RS-4 is N_2H_3 adsorbed on the fcc hollow site. The dehydrogenation process proceeds similarly with the the one previously

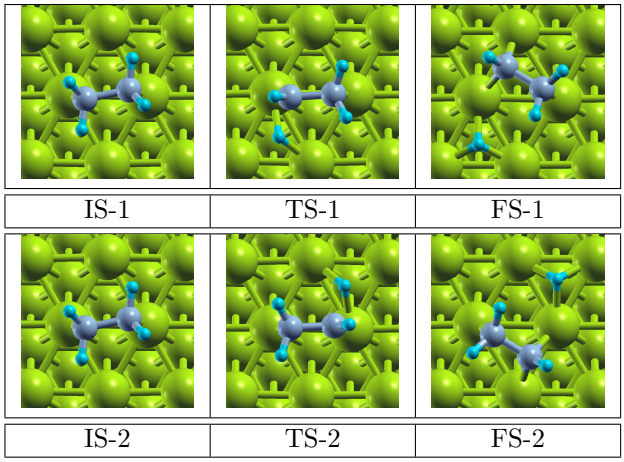

Figure 6.2: Reaction steps RS-1 and RS-2. In this figure and the following figures, we have used the labels IS-n, TS-n, and FS-n to signify initial, transition, and final state of reaction step RS-n.

mentioned. In the transition state, the broken H atom is adsorbed on the bridge site. In the final state, it will move to the fcc hollow site. The activation energy for RS-3 is lower (1.00 eV) than that for RS-4 (1.27 eV).

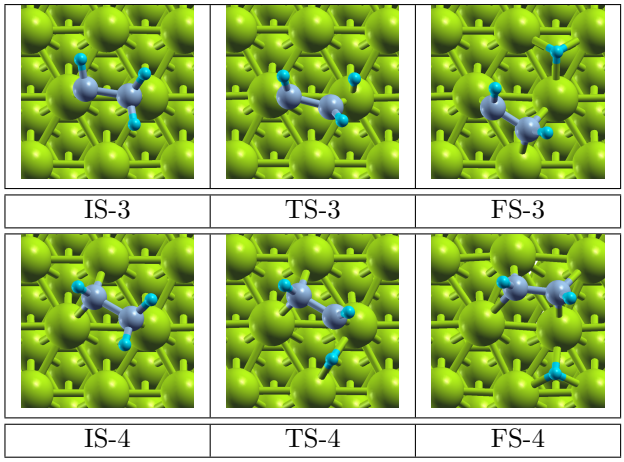

Figure 6.3: Reaction steps RS-3 and RS-4.

6.1.3 Third dehydrogenation

Three possibilities are considered here, namely the reaction steps RS-5, RS-6, and RS-7. The initial, transition, and final states of these reaction steps are shown in Figure 6.4. For reaction step RS-5, the initial state is N_2H_2 adsorbed on hcp hollow site that is similar to final state of RS-3. The dehydrogenation proceeds by the rotation of NH towards surface followed by N—H bond breaking. At transition state, the broken H atom adsorbs on the bridge site and moves to hcp hollow site. For reaction step RS-6, the initial state is similar to initial state of RS-5, but with both of the NH fragment of N_2H_2 are coordinated to two surfaces atoms. The dehydrogenation process proceeds similar with that of reaction step RS-5. Another alternative for third dehydrogenation is the reaction step RS-7. This reaction step is essentially similar to the reaction step RS-6 but with slightly different

final state. Despite these differences, the calculated activation energies for all these reaction steps are have values of about 1.00 eV.

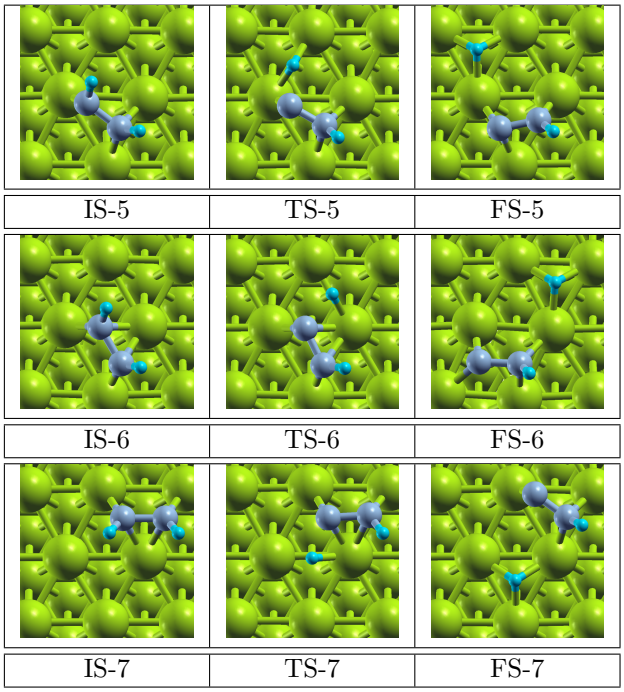

Figure 6.4: Reaction steps RS-5, RS-6, and RS-7.

6.1.4 Fourth dehydrogenation

One possibility is considered here, namely the reaction step RS-8. The initial, transition, and final states steps are shown in Figure 6.5. In the initial state the N_2H fragment is adsorbed on the hcp hollow site. The N_2H is adsorbed vertically with H atom bonded to the upper N atom. The dehydrogenation process proceed with the bending of N_2H towards surface followed by N—H bond breaking with H atom adsorbed on fcc hollow at the final state. This process also involves diffusion or movement of adsorbed N_2 from hcp hollow to top site. The calculated activation energy for this process is about 0.72 eV.

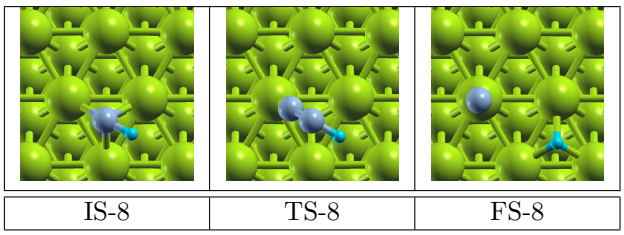

Figure 6.5: Reaction step RS-8.

6.1.5 Energy diagram

An energy diagram can be constructed for consecutive direct dehydrogenation reaction steps. An example is given in Figure 6.6 for reaction steps RS-1, RS-2, RS-5, and RS-8. To connect between final state of a reaction step with initial step of the next reaction, we assumed that the adsorbed hydrogen diffuses away or desorbs. Adsorption energy of H atom on fcc hollow site of -0.54 eV has been subtracted by going from final state of a reaction step to initial state of the next reaction step.

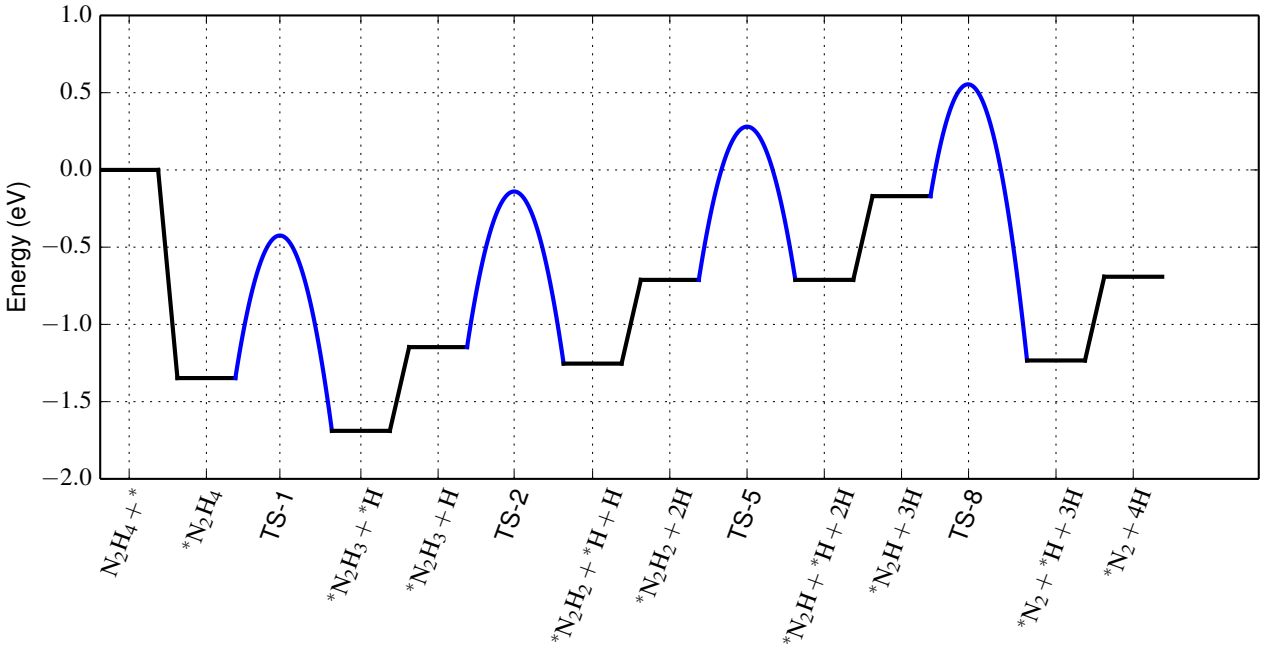

Figure 6.6: An energy diagram of direct dehydrogenation of hydrazine.

6.2 NH_2-assisted dehydrogenation: ammonia formation

A list of reaction steps with the corresponding activation energies are summarized in Table 6.2. The relative energies among different initial, transition, and final states of these reaction steps are shown in Figure 6.7. Comparison with 6.1 suggests that the NH_2-assisted dehydrogenation is preferable because it has lower activation energies as compared to the direct dehydrogenation.

6.2.1 First ammonia formation

One possibility is considered, namely the reaction step RS-9. The initial, transition, and final states of this reaction steps are shown in Figure 6.8. The initial state of RS-9 consists of hydrazine and nearby NH_2, both are adsorbed on bridge sites. The dehydrogenation process proceed by movement of NH_2 towards hydrazine and followed by H atom transfer from hydrazine to NH_2. The final state consists of N_2H_3 which is adsorbed on bridge site and NH_3 which is adsorbed on top site. The activation energy of this step is 0.33 eV which is lower than that for first direct dehydrogenation.

Here, we also include a calculation of activation barrier of the resulting ammonia to move away from N_2H_3. This is important because in order to prevent transfer of hydrogen atom from ammonia

Table 6.2: List of the considered reaction steps for NH_2-assisted dehydrogenation of hydrazine. Note that we also include NH_3 diffusion after the first NH_3 formation.

Reaction step	E_{act} (eV)
RS-9: $N_2H_4 + NH_2 \longrightarrow N_2H_3 + NH_3$	0.33
RS-10: NH_3 diffusion	0.68
RS-11: $N_2H_3 + NH_2 \longrightarrow N_2H_2 + NH_3$	0.50
RS-12: $N_2H_3 + NH_2 \longrightarrow N_2H_2 + NH_3$	0.32
RS-13: $N_2H_3 + NH_2 \longrightarrow N_2H_2 + NH_3$	0.40
RS-14: $N_2H_2 + NH_2 \longrightarrow N_2H + NH_3$	0.26
RS-15: $N_2H_2 + NH_2 \longrightarrow N_2H + NH_3$	0.45
RS-16: $N_2H + NH_2 \longrightarrow N_2 + NH_3$	0.39

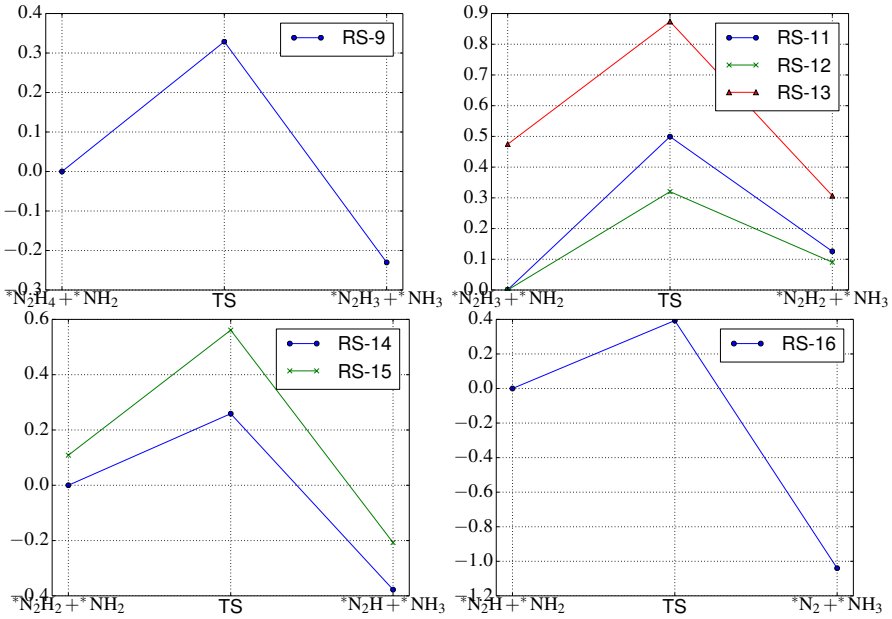

Figure 6.7: Relative energies among the NH_2-assisted dehydrogenation reaction steps. The energy of the most stable structure for each step is shifted to 0 eV.

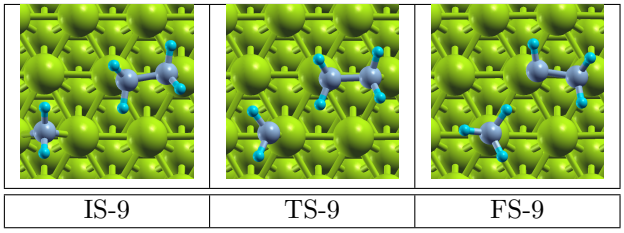

Figure 6.8: Reaction step RS-9.

back to N_2H_3, the resulting ammonia should diffuse away from N_2H_3. We designate this step as RS-10. The initial, transition, and final states of this reaction step are shown in Figure 6.9. The activation energy for this step is about 0.68 eV. This can be compared with activation energy for adsorbed hydrogen which is the product of direct dehydrogenation. From previous study [79], it is found that for Ni(111) activation energy for H atom diffusion is about 0.15 eV. This value is

significantly lower than that of ammonia diffusion. Even tough we do not explore this effect further, it is important to note that the difference might affect the overall reaction kinetics.

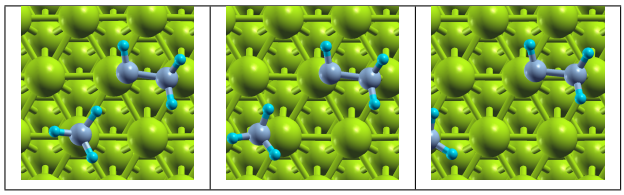

IS-10	TS-10	FS-10

Figure 6.9: Reaction step RS-10.

6.2.2 Second ammonia formation

Three possibilities are considered, namely the reactions steps RS-11, RS-12, and RS-13. The initial, transition, and final states of these reaction steps are shown in Figure 6.10. For RS-11, NH_2 takes hydrogen atom from the NH fragment of N_2H_3 adsorbed on fcc hollow site. For RS-12, NH_2 takes hydrogen atom from the NH_2 fragment of N_2H_3 adsorbed on fcc hollow site. Reaction step RS-13 is similar to RS-12 but with N_2H_3 adsorbed on bridge site. The calculated activation energies for these reaction steps are 0.50, 0.32, and 0.40 eV, respectively. The higher activation energy obtained for RS-11 might indicate that the N—H bond of the NH fragment is stronger than the N—H bond of the NH_2 fragment of N_2H_3.

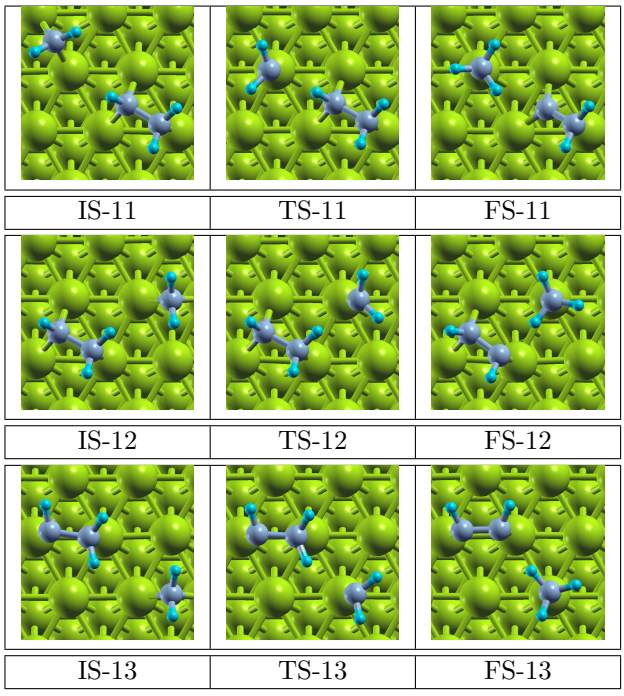

IS-11	TS-11	FS-11
IS-12	TS-12	FS-12
IS-13	TS-13	FS-13

Figure 6.10: Reaction steps RS-11, RS-12, and RS-13.

6.2.3 Third ammonia formation

Two possibilities are considered, namely the reactions steps RS-14 and RS-15. The initial, transition, and final states of these reaction steps are shown in Figure 6.11. For RS-14, the initial state consists of N_2H_2 adsorbed in the configuration similar to the final state of RS-11 and NH_2 adsorbed on bridge site. The dehydrogenation proceeds by movement of NH_2 to the top site near N_2H_2 followed by H atom transfer from N_2H_2 to NH_2. For RS-15, the initial state consists of N_2H_2 adsorbed in the configuration similar to the final state of RS-12 and also an NH_2 adsorbed on bridge site. The dehydrogenation process proceeds similarly with the previously discussed reaction steps. The calculated activation energies for these reaction steps are 0.26 and 0.45 eV, respectively. The lower value obtained for RS-14 is expected due to weaker N—H bond in NH_2 fragment of N_2H_2 as compared to N—H bond in NH fragment.

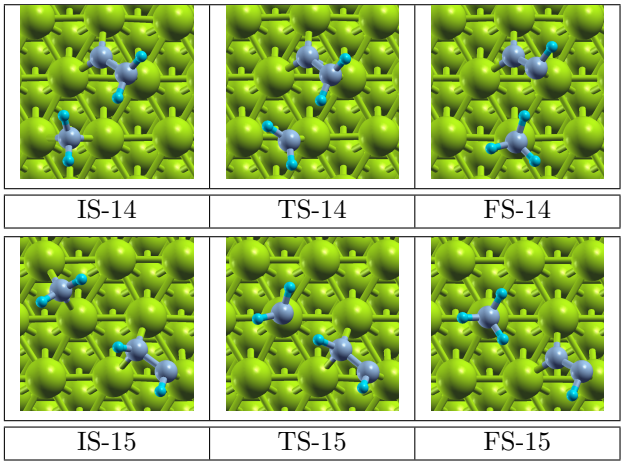

Figure 6.11: Reaction steps RS-14 and RS-15.

6.2.4 Fourth ammonia formation

One possibility is considered here, namely the reaction step RS-16. The initial, transition, and final states of this reaction steps are shown in Figure 6.12. For RS-16 the initial state consists of N_2H adsorbed vertically on fcc hollow site and an NH_2 adsorbed on bridge site. The dehydrogenation proceeds by movement of NH_2 from bridge site to top site and bending of N_2H towards NH_2. At final state, the remaining N_2 is found to adsorb on bridge site and NH_3 on top site. The remaining N_2 will likely move to the top site which is the more stable adsorption site. The calculated activation energy for this process is 0.39 eV.

6.2.5 Energy diagram

An energy diagram can also be constructed for consecutive NH_2-assisted dehydrogenation reaction steps. The diagram is given in 6.13 for reaction steps RS-9, RS-11, RS-14, and R-16. To connect between final state a reaction step with initial step of the next reaction, we have assumed that the adsorbed ammonia diffuses away from N_2H_x (x = 1, 2, or 3). NH_3 adsorption energy on top site of -1.03 eV has been subtracted by going from final state of a reaction to initial state of the next

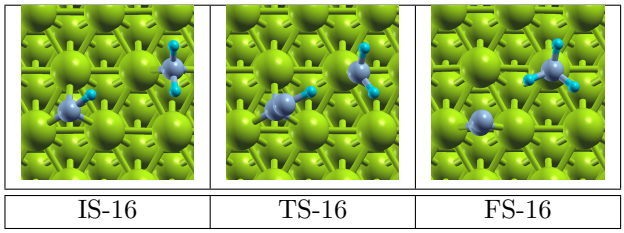

Figure 6.12: Reaction step RS-16.

reaction step. At the same time, adsorption energy of NH_2 on bridge site of -1.32 eV is also added, resulting in about 0.31 eV energy difference between final state of a reaction step and initial state of the next reaction step. This diagram may be compared with the one given in Figure 6.6. Our results are essentially similar to those found in the previous computational studies of hydrazine decomposition on Ir(111) [41] and Rh(111) [42]. It is also interesting to note that modeling the catalyst as cluster also lead to the same conclusion that NH_2-assisted dehydrogenation is preferred over direct dehydrogenation [78].

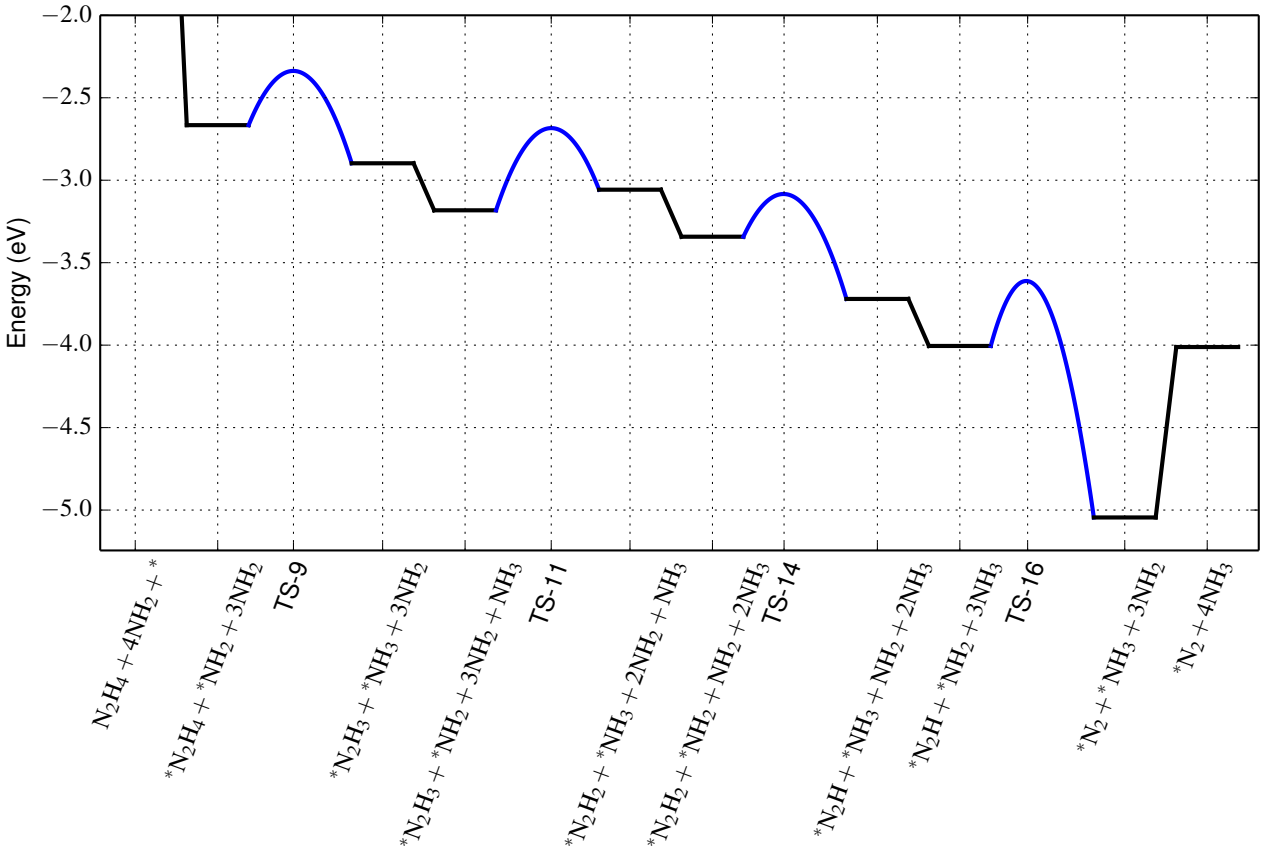

Figure 6.13: An energy diagram of NH_2-assisted dehydrogenation of hydrazine.

6.3 Chapter summary

Here, we give a list of important findings in this chapter.

- Two possible reaction pathways for dehydrogenation of hydrazine have been considered: the direct dehydrogenation and NH_2-assisted dehydrogenation pathways.
- The calculated activation energy of direct dehydrogenation of hydrazine ranges from 0.72–1.27 eV while for NH_2-assisted dehydrogenation it ranges from 0.26–0.50 eV. So, it can be said that the NH_2-assisted dehydrogenation is more favorable than the direct dehydrogenation.

The results are similar to the results of previous computational studies of hydrazine dehydrogenation on Ir(111) and Rh(111). On other surfaces that produce ammonia, the NH_2-assisted dehydrogenation is expected to be responsible for the ammonia formation. From the results, it is clear that ammonia formation is favorable on Ni(111) and NH_2-assisted dehydrogenation may be considered as the main reaction that lead to ammonia. To lower the production of ammonia, we should minimize the NH_2-assisted dehydrogenation. One way to do this is to lower the production of NH_2 or N—N bond cleaving.

CHAPTER 7

Concluding remarks

In this dissertation, we have investigated various aspects of hydrazine-metal surface reactions including the adsorption, comparison of N—N and first N—H bond cleaving, and dehydrogenation pathways of hydrazine on Ni(111) surface.

We have characterized adsorption configurations of hydrazine on close-packed surfaces of $3d$, $4d$, and $5d$ metals. The adsorption configurations may be classified into *top* and *bridging* configurations. It is found that on most surfaces hydrazine will adsorb in *bridging* configurations. Especially on the surfaces of metals that are located at the left side of the periodic table (early d metals), the difference of adsorption energies between *top* and *bridging* configurations are relatively large. However, the *top* configurations of hydrazine will be favored instead on surfaces of metals that are located at the right side of the periodic table (late d metals). Regarding the electronic structure, HOMO and HOMO-1 of hydrazine are found to dominate the interaction with the surface atoms. The results that we have obtained here are expected to be useful for future experimental works of hydrazine adsorption configurations on metal surfaces.

We also have investigated reactivity of several metal surfaces towards N—N and first N—H bond cleaving of hydrazine. For most surfaces, it is found that N—N bond cleaving is more favorable than the first N—H bond cleaving. The trend of activation energy for both N—N and N—H bond cleaving is found to be increasing as we go from the left to the right side of periodic table. By analyzing the electronic structure of hydrazine adsorbed on $3d$-metal surfaces, the trend is found to be related to the occupation of LUMO-derived orbitals of hydrazine in the transition state. The transition state for N—N bond cleaving can already be reached by simple N—N bond stretching. Meanwhile, for N—H bond cleaving, to reach the transition state NH_2 part of hydrazine needs to rotate towards the surface. This rotation can then be followed by N—H bond stretching. A more complex geometrical change required to reach the transition state of N—H as compared to N—N bond cleaving might be responsible for higher activation energy of N—H bond cleaving. Aside from these results, we also have established several BEP relationships for N—N and first N—H bond cleaving of hydrazine on various metal surfaces. This information is not yet available in the current literature and hopefully can be used to estimate the activation energy of N—N and first N—H bond cleaving of hydrazine on other systems, for example alloy surfaces.

Two dehydrogenation pathways of hydrazine have been investigated on Ni(111) surface: the direct and NH_2-assisted dehydrogenation. In direct dehydrogenation, the N—H bonds of hydrazine are cleaved directly, which results in H atom adsorption on the surface. In NH_2-assisted dehydro-

genation, the N—H bonds of hydrazine are cleaved by H transfer from hydrazine to the adsorbed NH_2 fragments, which results in ammonia formation. It is found that the NH_2-assisted dehydrogenation is favored over direct dehydrogenation pathway. The results suggests that NH_3 formation is favorable on Ni(111) surface. The results are similar to the results of previous computational studies of hydrazine dehydrogenation on Ir(111) and Rh(111). On other surfaces that produce ammonia, the NH_2-assisted dehydrogenation is expected to be responsible for the ammonia formation.

From the result that we have obtained, we can suggest a way to lower the quantity of ammonia from the decomposition of hydrazine. One might think that choosing the surfaces with low activation energy of N—H bond cleaving will reduce the production of ammonia. However, from the findings in this study, it is found that surfaces with low N—H activation energy will also have low activation energy for N—N bond cleaving. For all surfaces that are considered here, N—N bond cleaving will be more favorable than N—H bond cleaving. Therefore, just choosing surfaces with low N—H activation energy will not necessary lead to low ammonia production or even high performance of hydrogen production. Instead, it is suggested to choose a metal that has high N—N activation energy or difficult to produce NH_2. Example of such metal is Zn. This metal can then be alloyed with metal which has intermediate reactivity toward N—H, such as Ni. The NiZn catalyst has been tested as catalyst for direct hydrazine fuel cell [77]. This catalyst is found to have high performance due low NH_3 production.

Bibliography

[1] Yamada, K., Yasuda, K., Tanaka, H., Miyazaki, Y. and Kobayashi, T. *J. Power Sources*, **122** (2003):132 – 137.

[2] Asazawa, K., Yamada, K., Tanaka, H., Oka, A., Taniguchi, M. and Kobayashi, T. *Angew. Chem. Int. Ed.*, **46** (2007):8024–8027.

[3] Asazawa, K., Sakamoto, T., Yamaguchi, S., Yamada, K., Fujikawa, H., Tanaka, H. and Oguro, K. *J. Electrochem. Soc.*, **156** (2009):B509–B512.

[4] Serov, A. and Kwak, C. *Appl. Catal., B: Environmetal*, **98** (2010):1–9.

[5] Yang, H., Zhong, X., Dong, Z., Wang, J., Jin, J. and Ma, J. *RSC Adv.*, **2** (2012):5038–5040.

[6] Zheng, M., Cheng, R., Chen, X., Li, N., Li, L., Wang, X. and Zhang, T. *Int. J. Hydrogen Energy*, **30** (2005):1081–1089.

[7] Singh, S.K., Zhang, X.B. and Xu, Q. *J. Am. Chem. Soc.*, **131** (2009):9894–9895.

[8] Singh, S.K. and Xu, Q. *Catal. Sci. Technol.*, **3** (2013):1889–1900.

[9] Batonneau, Y., Kappenstein, C.J. and Keim, W. In G. Ertl, H. Knözinger and J. Weitkamp (Editors) *Handbook of Heterogeneous Catalysis*. VCH Verlagsgesellschaft mbH, 2008.

[10] Furst, A., Berlo, R.C. and Hooton, S. *Chem. Rev.*, **65** (1965):51–68.

[11] Audrieth, L.F. and Ogg, B.A. *The Chemistry of Hydrazine*. Wiley, 1951.

[12] Aika, K., Ohhata, T. and Ozaki, A. *J. Catal.*, **19** (1970):140–143.

[13] Maurel, R. and Menezo, J. *J. Catal.*, **51** (1978):293–295.

[14] Contaminard, R.C.A. and Tompkins, F.C. *Trans. Faraday Soc.*, **67** (1971):545–555.

[15] Cosser, R.C. and Tompkins, F.C. *Trans. Faraday Soc.*, **67** (1971):526–544.

[16] Contour, J. and Pannetier, G. *J. Catal.*, **24** (1972):434–445.

[17] Johnson, D. and Roberts, M. *J. Electron. Spectrosc. Relat. Phenom.*, **19** (1980):185–195.

[18] Gland, J.L., Fisher, G.B. and Mitchell, G.E. *Chem. Phys. Lett.*, **119** (1985):89–92.

[19] Daniel, W. and White, J. *Surf. Sci.*, **171** (1986):289–302.

[20] Prasad, J. and Gland, J.L. *Langmuir*, **7** (1991):722–726.

[21] Prasad, J. and Gland, J.L. *Surf. Sci.*, **258** (1991):67–74.

[22] Dopheide, R., Schröter, L. and Zacharias, H. *Surf. Sci.*, **257** (1991):86–96.

[23] Wagner, M. and Schmidt, L.D. *Surf. Sci.*, **257** (1991):113–128.

[24] Alberas, D.J., Kiss, J., Liu, Z.M. and White, J. *Surf. Sci.*, **278** (1992):51–61.

[25] Huang, S.X., Rufael, T.S. and Gland, J.L. *Surf. Sci. Lett.*, **290** (1993):L673–L676.

[26] Rauscher, H., Kostov, K. and Menzel, D. *Chem. Phys.*, **177** (1993):473–496.

[27] Lee, S., Fan, C., Wu, T. and Anderson, S.L. *J. Phys. Chem. B*, **109** (2005):381–388.

[28] Fan, C., Wu, T., Kaden, W.E. and Anderson, S.L. *Surf. Sci.*, **600** (2006):461–467.

[29] Apen, E. and Gland, J.L. *Surf. Sci.*, **321** (1994):308–317.

[30] Bu, Y. and Lin, M. *Surf. Sci.*, **311** (1994):385–394.

[31] Chen, X., Zhang, T., Zheng, M., Wu, Z., Wu, W. and Li, C. *J. Catal.*, **224** (2004):473–478.

[32] Bu, Y., Shinn, D. and Lin, M. *Surf. Sci.*, **276** (1992):184–199.

[33] Zheng, M., Chen, X., Cheng, R., Li, N., Sun, J., Wang, X. and Zhang, T. *Catal. Commun.*, **7** (2006):187–191.

[34] Sun, J., Zheng, M., Wang, X., Wang, A., Cheng, R., Li, T. and Zhang, T. *Catal. Lett.*, **123** (2008):150–155.

[35] Daff, T.D., Costa, D., Lisiecki, I. and de Leeuw, N.H. *J. Phys. Chem. C*, **113** (2009):15714–15722.

[36] Agusta, M.K., David, M., Nakanishi, H. and Kasai, H. *Surf. Sci.*, **604** (2010):245–251.

[37] Agusta, M.K., Dino, W.A., David, M., Nakanishi, H. and Kasai, H. *Surf. Sci.*, **605** (2011):1347–1353.

[38] Agusta, M.K. and Kasai, H. *Surf. Sci.*, **606** (2012):766–771.

[39] Agusta, M.K. and Kasai, H. *J. Phys. Soc. Jpn*, **81** (2012):124705.

[40] McKay, H.L., Jenkins, S.J. and Wales, D.J. *J. Phys. Chem. C*, **115** (2011):17812–17828.

[41] Zhang, P.X., Wang, Y.G., Huang, Y.Q., Zhang, T., Wu, G.S. and Li, J. *Catal. Today*, **165** (2011):80–88.

[42] Deng, Z., Lu, X., Wen, Z., Wei, S., Liu, Y., Fu, D., Zhao, L. and Guo, W. *Phys. Chem. Chem. Phys.*, **15** (2013):16172–16182.

[43] Hohenberg, P. and Kohn, W. *Phys. Rev.*, **136** (1964):864–871.

[44] Kohn, W. and Sham, L. *Phys. Rev.*, **140** (1965):1133–1138.

[45] Jónsson, H., Mills, G. and Jacobsen, K.W. In B.J. Berne, G. Ciccotti and D.F. Coker (Editors) *Classical and Quantum Dynamics in Condensed Phase Simulations*. World Scientific, 1998.

[46] Henkelman, G. and Jónsson, H. *J. Chem. Phys.*, **113** (2000):9978–9985.

[47] Henkelman, G., Uberuaga, B.P. and Jónsson, H. *J. Chem. Phys.*, **113** (2000):9901–9904.

[48] Giannozzi, P., Baroni, S., Bonini, N., Calandra, M., Car, R., Cavazzoni, C., Ceresoli, D., Chiarotti, G.L., Cococcioni, M., Dabo, I., Dal Corso, A., de Gironcoli, S., Fabris, S., Fratesi, G., Gebauer, R., Gerstmann, U., Gougoussis, C., Kokalj, A., Lazzeri, M., Martin-Samos, L., Marzari, N., Mauri, F., Mazzarello, R., Paolini, S., Pasquarello, A., Paulatto, L., Sbraccia, C., Scandolo, S., Sclauzero, G., Seitsonen, A.P., Smogunov, A., Umari, P. and Wentzcovitch, R.M. *J. Phys. Condens. Matter*, **21** (2009):395502. Code available from `http://www.quantum-espresso.org`.

[49] Vanderbilt, D. *Phys. Rev. B*, **41** (1990):7892–7895.

[50] Marzari, N., Vanderbilt, D., De Vita, A. and Payne, M.C. *Phys. Rev. Lett.*, **82** (1999):3296–3299.

[51] Bahn, S. and Jacobsen, K. *Comput. Sci. Eng.*, **4** (2002):56–66. Code available from `http://wiki.fysik.dtu.dk/ase`.

[52] Perdew, J.P., Burke, K. and Ernzerhof, M. *Phys. Rev. Lett.*, **77** (1996):3865–3868.

[53] Janthon, P., Kozlov, S.M., Viñes, F., Limtrakul, J. and Illas, F. *J. Chem. Theory Comput.*, **9** (2013):1631–1640.

[54] Janthon, P., Luo, S.A., Kozlov, S.M., Viñes, F., Limtrakul, J., Truhlar, D.G. and Illas, F. *J. Chem. Theory Comput.*, **10** (2014):3832–3839.

[55] Grimme, S. *J. Comput. Chem.*, **27** (2006):1787–1799.

[56] Barone, V., Casarin, M., Forrer, D., Pavone, M., Sambi, M. and Vittadini, A. *J. Comput. Chem.*, **30** (2009):934–939.

[57] Grimme, S., Antony, J., Ehrlich, S. and Krieg, H. *J. Chem. Phys.*, **132** (2010):154104.

[58] Tafreshi, S.S., Roldan, A., Dzade, N.Y. and de Leeuw, N.H. *Surf. Sci.*, **622** (2014):1–8.

[59] Frisch, M.J., Trucks, G.W., Schlegel, H.B., Scuseria, G.E., Robb, M.A., Cheeseman, J.R., Scalmani, G., Barone, V., Mennucci, B., Petersson, G.A., Nakatsuji, H., Caricato, M., Li, X., Hratchian, H.P., Izmaylov, A.F., Bloino, J., Zheng, G., Sonnenberg, J.L., Hada, M., Ehara, M., Toyota, K., Fukuda, R., Hasegawa, J., Ishida, M., Nakajima, T., Honda, Y., Kitao, O., Nakai, H., Vreven, T., Montgomery, Jr., J.A., Peralta, J.E., Ogliaro, F., Bearpark, M., Heyd,

J.J., Brothers, E., Kudin, K.N., Staroverov, V.N., Kobayashi, R., Normand, J., Raghavachari, K., Rendell, A., Burant, J.C., Iyengar, S.S., Tomasi, J., Cossi, M., Rega, N., Millam, J.M., Klene, M., Knox, J.E., Cross, J.B., Bakken, V., Adamo, C., Jaramillo, J., Gomperts, R., Stratmann, R.E., Yazyev, O., Austin, A.J., Cammi, R., Pomelli, C., Ochterski, J.W., Martin, R.L., Morokuma, K., Zakrzewski, V.G., Voth, G.A., Salvador, P., Dannenberg, J.J., Dapprich, S., Daniels, A.D., Farkas, O., Foresman, J.B., Ortiz, J.V., Cioslowski, J. and Fox, D.J. Gaussian09 Revision C.01. Gaussian Inc. Wallingford CT 2009.

[60] Kokalj, A. *Comp. Mater. Sci.*, **28** (2003):155–168. Code available from `http://www.xcrysden.org/`.

[61] Hunter, J.D. *Comput. Sci. Eng.*, **9** (2007):90–95.

[62] Hammer, B. and Nørskov, J. *Surf. Sci.*, **343** (1995):211–220.

[63] Hammer, B., Morikawa, Y. and Nørskov, J. *Phys. Rev. Lett.*, **76** (1996):2141.

[64] Grunze, M. *Surf. Sci.*, **81** (1979):603–625.

[65] Cao, Y. and Chen, Z.X. *Phys. Chem. Chem. Phys.*, **9** (2007):739–746.

[66] Li, S., Lu, X., Guo, W., Zhu, H., Li, M., Zhao, L., Li, Y. and Shan, H. *J. Organomet. Chem.*, **704** (2012):38–48.

[67] Brønsted, J. and Pedersen, K. *Z. Phys. Chem.*, **108** (1924):185–235.

[68] Evans, M.G. and Polanyi, M. *Trans. Faraday Soc.*, **32** (1936):1333–1360.

[69] Michaelides, A., Liu, Z.P., Zhang, C., Alavi, A., King, D.A. and Hu, P. *J. Am. Chem. Soc.*, **125** (2003):3704–3705.

[70] Toulhoat, H. and Raybaud, P. *J. Catal.*, **216** (2003):63–72.

[71] Bligaard, T., Nørskov, J., Dahl, S., Matthiesen, J., Christensen, C. and Sehested, J. *J. Catal*, **224** (2004):206 – 217.

[72] Menning, C.A. and Chen, J.G. *J. Chem. Phys.*, **128** (2008).

[73] Huang, S.C., Lin, C.H. and Wang, J.H. *J. Phys. Chem. C*, **114** (2010):9826–9834.

[74] van Santen, R.A., Neurock, M. and Shetty, S.G. *Chem. Rev.*, **110** (2010):2005–2048.

[75] Wang, S., Temel, B., Shen, J., Jones, G., Grabow, L.C., Studt, F., Bligaard, T., Abild-Pedersen, F., Christensen, C.H. and Norskov, J.K. *Catal. Lett.*, **141** (2011):370–373.

[76] Fajín, J.L., Cordeiro, M.N.D., Illas, F. and Gomes, J.R. *J. Catal.*, **313** (2014):24 – 33.

[77] Martinez, U., Asazawa, K., Halevi, B., Falase, A., Kiefer, B., Serov, A., Padilla, M., Olson, T., Datye, A., Tanaka, H. and Atanassov, P. *Phys. Chem. Chem. Phys.*, **14** (2012):5512–5517.

[78] Schmidt, M.W. and Gordon, M.S. *Z. Phys. Chem.*, **227** (2013):1301–1336.

[79] Kristinsdóttir, L. and Skúlason, E. *Surf. Sci.*, **606** (2012):1400–1404.

[80] Garrity, K.F., Bennett, J.W., Rabe, K.M. and Vanderbilt, D. *Comp. Mat. Sci,*, **81** (2014):446–452.

APPENDIX A

List of used pseudopotentials

The Quantum ESPRESSO package has a database of various pseudopotentials. Most of these pseudopotentials are standard and can be found on the website of Quantum ESPRESSO. However, for some elements the appropriate pseudopotentials are not available, so we also used the pseudopotentials from the GBRV (Garrity-Bennett-Rabe-Vanderbilt) database [80]. In Table A.1, the GBRV pseudopotentials are identified by `.v1.` in their file names.

Table A.1: List of pseudopotentials used in this work.

Element	File name
Sc	`Sc.pbe-nsp-van.UPF`
Ti	`Ti.pbe.v1.uspp.F.UPF`
V	`V.pbe.v1.uspp.F.UPF`
Cr	`Cr.pbe.v1.uspp.F.UPF`
Fe	`Fe.pbe-sp-van_ak.UPF`
Co	`Co.pbe-nd-rrkjus.UPF`
Ni	`Ni.pbe-nd-rrkjus.UPF`
Cu	`Cu.pbe-n-van_ak.UPF`
Zn	`Zn.pbe-van.UPF`
Y	`Y.pbe.v1.uspp.F.UPF`
Zr	`Zr.pbe-nsp-van.UPF`
Nb	`Nb.pbe-nsp-van.UPF`
Mo	`Mo.pbe.v1.uspp.F.UPF`
Ru	`Ru.pbe-n-van.UPF`
Rh	`Rh.pbe-nd-rrkjus.UPF`
Pd	`Pd.pbe-nd-rrkjus.UPF`
Ag	`Ag.pbe-d-rrkjus.UPF`
La	`La.pbe-nsp-van.UPF`
Ta	`Ta.pbe-nsp-van.UPF`
Hf	`Hf.pbe.v1.F.UPF`
W	`W.pbe-nsp-van.UPF`
Re	`Re.pbe.v1.uspp.F.UPF`
Os	`Os.pbe.v1.uspp.F.UPF`
Ir	`Ir.pbe-n-rrkjus.UPF`
Pt	`Pt.pbe-nd-rrkjus.UPF`
Au	`Au.pbe-nd-rrkjus.UPF`

APPENDIX B

Calculation of molecular-orbital-projected density of states

In this appendix, we describe the procedure on how to obtain projection to molecular orbitals. Given a set of orbitals $\{|\Psi_{i,\mathbf{k}}\rangle\}$ of composite system, which consists of for example surface and a molecule Suppose that this orbitals can be expanded using atomic-centered orbitals $|\phi_a\rangle$, with $a = 1, \ldots, N_a$

$$|\Psi_{i,\mathbf{k}}\rangle = \sum_{a}^{N_a} c_{i,a} |\phi_a\rangle \tag{B.1}$$

We want to project $|\Psi_{j,\mathbf{k}}\rangle$ to a set of molecular orbitals $\{|\psi_{j,\mathbf{k}}\rangle\}$ of the subsystem, for example the molecule, with $j = 1, \ldots, N_{MO}$. This subsystem is constrained to have similar periodicity with the composite system. This molecular orbitals also can be expanded in atomic centered orbitals $\{|\phi_{a'}\rangle\}$:

$$|\psi_{j,\mathbf{k}}\rangle = \sum_{a'}^{N_{a'}} c_{j,a'} |\phi_{a'}\rangle \tag{B.2}$$

where $N_{a'} \leq N_a$ and a' used as index of subset of atomic molecular orbitals used to expand the composite system. The coefficients $c_{i,a}$ and $c_{j,a'}$ can be calculated using the utility `projwfc.x` of the Quantum Espresso distribution.

The orbitals of $\{|\Psi_{i,\mathbf{k}}\rangle\}$ can be expanded by using the molecular orbitals $|\psi_{j,\mathbf{k}}\rangle$ of the subsystem as follows

$$|\Psi_{i,\mathbf{k}}\rangle = \sum_{j}^{N_{MO}} c_{i,j,\mathbf{k}} |\psi_{j,\mathbf{k}}\rangle \tag{B.3}$$

with the expansion coefficients

$$c_{i,j,\mathbf{k}} = \langle \Psi_{i,\mathbf{k}} | \psi_{j,\mathbf{k}} \rangle \tag{B.4}$$

$$= \sum_{a'}^{N_{a'}} c^*_{i,a'} c_{j,a'} \tag{B.5}$$

A more important quantity is

$$|c_{i,j,\mathbf{k}}|^2 = \sum_{a'}^{N_{a'}} c^*_{i,a'} c_{j,a'} \sum_{a'}^{N_{a'}} c^*_{j,a'} c_{i,a'} \tag{B.6}$$

This quantity can be used to calculate MO-projected density of states. We have followed the subroutine `partialdos` in the file `PP/src/projwfc.f90` of Quantum Espresso distribution to calculate the density of states from $\left|c_{i,j,\mathbf{k}}\right|^2$.

APPENDIX C

Long and short bridge sites of bcc(110) surfaces

On bcc(110) surfaces, such as Fe(110), there are two possible adsorption sites for hydrazine, namely the short and long bridge sites. In this appendix, we will discuss an example of how structure affects the reactivity of surface towards N—N bond cleaving of hydrazine. From NEB calculations it was found that short bridge site has higher activation energy than long bridge site. Here we illustrate the effect for the case of Fe(110) surface. This effect also can be found on other bcc(110) surfaces such as Mo(110) and Nb(110). The activation energies at the long and short bridge sites for those surfaces are given in Table C.1. Note that we will add the suffix *-lb* to label the adsorption on long bridge site and *-sb* for adsorption on short bridge site.

Table C.1: Comparison of N—N activation energy on long and short bridge sites of several bcc(110) surfaces.

Surface	long bridge	short bridge
Fe(110)	0.23	0.31
Nb(110)	0.19	0.26
Mo(110)	0.22	0.26

In order to find the origin of this activation energy difference, the electronic structure of configurations *bri-A-lb* and *bri-A-sb* will be analyzed and compared. Figure C.1 shows the density of states projected on p_x, p_y and p_z of N atom when the adsorption configuration is *bri-A-lb* and *bri-A-sb*. It is found that both plots have very similar features. There is not much difference in the corresponding p_z components (blue line), so the activation energy difference should be related to the p_x and p_y components of DOS. Four peaks (states) of DOS for each *bri-A-lb* and *bri-A-sb* are given labels A, B, C, and D. The corresponding molecular orbitals of on these peaks are also given in Figure C.1.

It can be seen that the peak A of *bri-A-lb* corresponds to the σ bonding between the p_x orbitals of N atoms. The second peak corresponds to the π anti-bonding between the two NH_2 fragments. These two orbitals are essentially the same as 5σ and $2\pi^*$ orbitals of gas phase hydrazine in *cis* conformation. The third and fourth peaks both have N—N bonding characters. They are the result of the interaction between HOMO-1 and surface atom orbitals. Thus, on long bridge site there are three bonding and one anti-bonding states among the 4 states that were considered. First peak of *bri-A-sb* has the same character as in the long bridge, i.e. it is a σ bonding between N—N atoms, although now it is composed not purely of p_x but also of p_y orbitals. However, the second

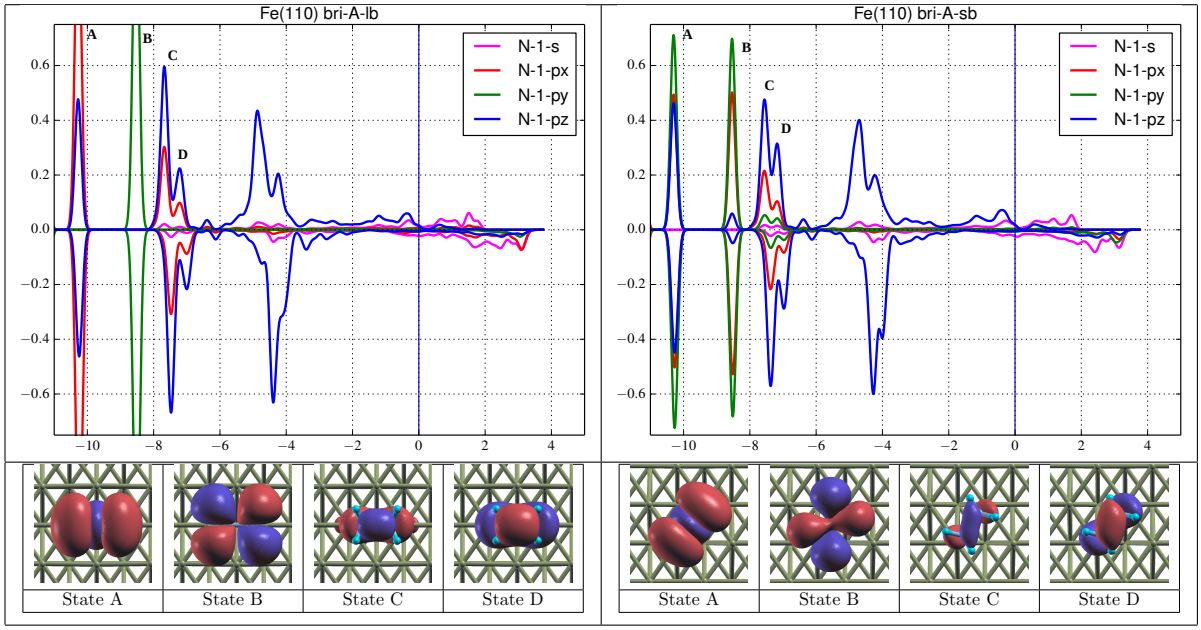

Figure C.1: Electronic structure of hydrazine adsorbed on long and short bridge of Fe(110).

peak of this configuration is not π anti-bonding as we can see slight bonding character between H atoms belonging to different NH_2 fragments. Similarly to the case of long bridge, third and fourth peaks are also result of the interaction between HOMO-1 and surface atom orbitals which have bonding characteristic. Thus, on the short bridge site all four states that were considered have bonding characteristic. Qualitatively, it can be said that the bonding between two NH_2 fragments of adsorbed hydrazine in short bridge is stronger as compared to the long bridge site. This will eventually result in higher activation energy of N—N bond cleaving for short bridge.

Another difference between long and short bridge sites is that the adsorption energy on short bridge site is generally larger (more negative) than similar adsorption on long bridge site. The origin of this difference also can be attributed to the previously described electronic structure aspects. State B of short bridge site is found to have contribution from p_z of N atom which means that it interact with surface. As opposed to state B of long bridge, state B of short bridge has bonding character with surface which can be deduced from Figure C.2.

Table C.2: Comparison of *bri-A* adsorption energy on long and short bridge sites of several bcc(110) surfaces.

Surface	long bridge	short bridge
Fe(110)	-1.28	-1.38
Nb(110)	-1.73	-1.82
Mo(110)	-1.72	-1.97

For Nb(110) and Mo(110), these kind of electronic states also may be found. These are shown in Figures C.3 and C.4 for Nb(110) and Mo(110), respectively. For other bcc(110), similar electronic structures are also expected to be found.

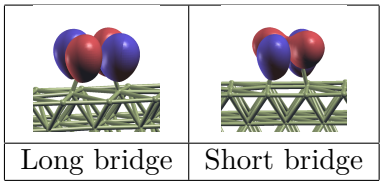

Figure C.2: Visualization of state B, which is similar to $2\pi^*$ MO of hydrazine in gas phase, of long and short bridge sites. On long bridge site, this state is not interact with surface while on short bridge site we can observe polarization of this MO towards surface.

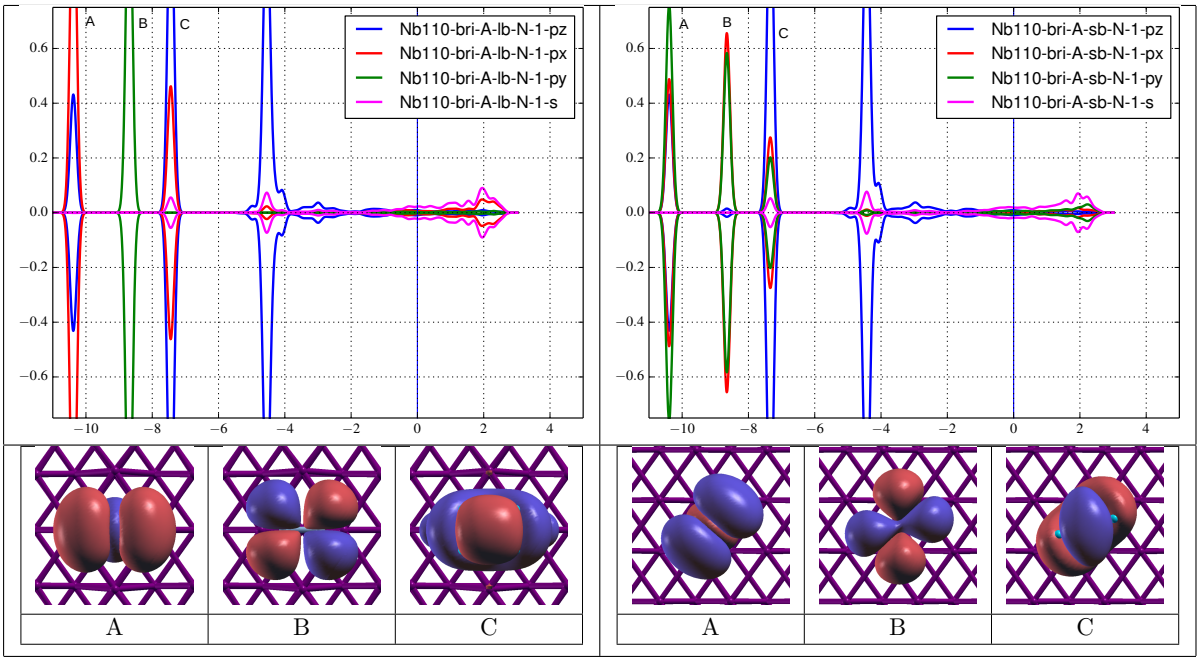

Figure C.3: Electronic structure of hydrazine adsorbed on long and short bridge of Nb(110).

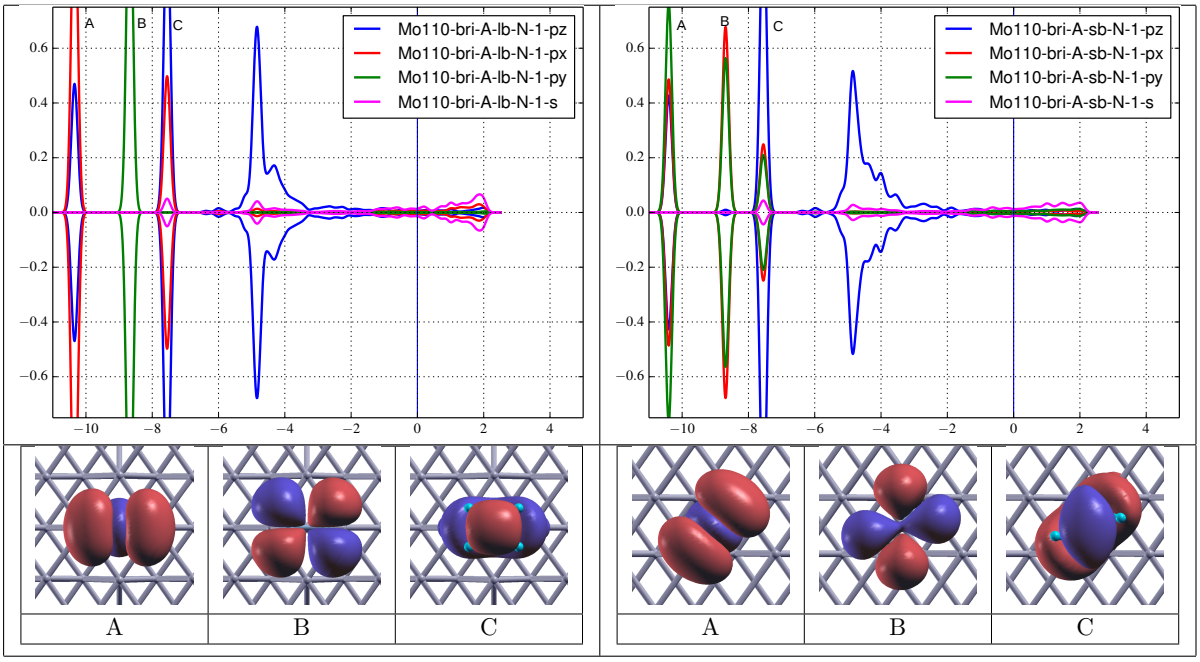

Figure C.4: Electronic structure of hydrazine adsorbed on Mo(110).

Acknowledgment

I am extremely grateful to my advisor, Wilson Agerico Diño, for his continuing support. I am also extremely grateful to my dissertation committee members for their guidance and patience: Prof. Yasuhiro Sugawara, Prof. Eiichi Tamiya, Prof. Tamio Oguchi, and Prof. Hideaki Kasai.

I am thankful to my lab members for their help during my stay in Japan.

I wish to be able thank my late father. I would like to thank my mother, my younger brothers and my sister for their extreme patience and understanding.

Some of the numerical calculations presented here were done using the computer facilities at the following institutes: CMC (Osaka University), ISSP, KEK, NIFS, and YITP.

I gratefully acknowledge the scholarship support from the Japan International Cooperation Agency (JICA) for the development of Institute of Technology Bandung program.

Publications

1. Density Functional Study of Hydrazine Adsorption and Its N—N Bond Cleaving on Fe(110) Surface. Fadjar Fathurrahman and Hideaki Kasai. *Surf. Sci.* **639** (2015) 25–31. Selected to appear on the journal cover.

2. Density Functional Study of Hydrazine N—N Bond Cleaving on 3*d* Metal Surfaces. Fadjar Fathurrahman and Hideaki Kasai. *Surf. Sci.* **641** (2015) 191–197.

3. Computational Study of Hydrazine Adsorption on Close-Packed Metal Surfaces of *d*-block Metals. Fadjar Fathurrahman and Hideaki Kasai, in preparation.

4. Computational Study of Hydrazine Decomposition Reactions Pathways on Ni(111). Fadjar Fathurrahman and Hideaki Kasai, in preparation.

Presentation in Scientific Meetings

1. Hydrazine N—N Bond Cleaving Process on Transition Metal Surfaces, Fadjar Fathurrahman, QEDC Workshop February 2014. (Oral)

2. Hydrazine N—N Bond Breaking Process on Transition Metal Surfaces, Fadjar Fathurrahman and Hideaki Kasai, International Workshop Atomically Controlled Fabrication Technology, 5–6 February 2014, Osaka, Japan. (Poster)

3. Density Functional Study of Hydrazine Adsorption and N—N Bond Cleaving on Fe(110) Surface, Fadjar Fathurrahman and Hideaki Kasai, Vacuum Society of Japan 55th Conference, 2014, 18–20 November 2014, Osaka, Japan. (Poster)

4. Theoretical Study of Hydrazine Decomposition on Ni(111) Surface, Fadjar Fathurrahman, QEDC Workshop 5 February 2015. (Oral)

Biography

Birth

29 September 1988, Pekanbaru, Riau, Indonesia

Education

- (1994-2000) Elementary School, Pekanbaru, Riau, Indonesia
- (2000-2003) Middle School, Pekanbaru, Riau, Indonesia
- (2003-2006) High School, Pekanbaru, Riau, Indonesia
- (2006-2010) Bachelor of Engineering, Department of Engineering Physics, Bandung Institute of Technology, Bandung, Indonesia
- (2010-2012) Master of Science, Department of Computational Science, Bandung Institute of Technology, Indonesia
- (2012-2015) Department Applied Physics & Precision Science, Graduate School of Engineering, Osaka University, Japan

Scholarship

Japan International Cooperation Agency (JICA) through ITB development program